Research on Stable, High-Efficiency Amorphous Silicon Multijunction Modules

Annual Subcontract Report
1 January 1992 – 28 February 1993

S. Guha
United Solar Systems Corporation
Troy, Michigan

NREL technical monitor: W. Luft

◆NREL

MASTER

NOTICE

DISCLAIMER

Portions of this document may be illegible electronic image products. Images are produced from the best available original document.

Preface

This Annual Subcontract Report covers the work performed by United Solar Systems Corp. for the period 1 January 1992 to 28 February 1993 under DOE/NREL Subcontract Number ZM-1-19033-2. The following personnel participated in the research program.

A. Banerjee, E. Chen, R. Clough, T. Glatfelter, S. Guha (Principal Investigator), G. Hammond, K. Hoffman, M. Hopson, N. Jackett, M. Lycette, J. Noch, T. Palmer, K. Parker, I. Rosenstein, D. Wolf, J. Yang, X. Xu and K. Younan.

The small-angle X-ray scattering experiments reported in Section 3 were carried out at the Colorado School of Mines by D. L. Williamson, S. J. Jones and Y. Chen, and we thank them for this collaborative effort.

We would like to thank V. Trudeau for preparation of this report.

Table of Contents

List of Figures

iv

List of Tables

Executive Summary

Objectives

The principal objective of the program is to conduct research on semiconductor materials and non-semiconductor materials to enhance the performance of multi-bandgap, multijunction, large-area amorphous silicon-based alloy modules. The goal for Phase II is to demonstrate stabilized module efficiency of 10% for multijunction panel of area greater than 900 cm^2.

Approach

Double-junction and triple-junction cells are made on Ag/ZnO back reflector deposited on stainless steel substrates. a-SiGe alloy is used for the i layer in the bottom and the middle cells; the top cell uses a-Si alloy. After evaporation of antireflection coating, silver grids and bus bars are put on the top surface, and the panel is encapsulated in an ethylene vinyl acetate (EVA)/Tefzel structure to make a one-square-foot monolithic module.

Status/Accomplishments

- Using a combination of small-angle scattering and infrared absorption measurements on a-Si alloy films and efficiency measurements on cells, we find that there is a correlation between the microstructure of the films and cell performance. Both the initial and the stabilized performance of solar cells deteriorate when the microvoid density in the films becomes larger.

- The annealing kinetics of the metastable defects is also found to depend on the density of microvoids in the films. With increasing microvoid density, some light-induced defects are created which are harder to anneal out.

- A detailed investigation of film property and cell performance using a-SiGe alloys with different germanium contents shows that there is no good correlation between defect density measured by the constant photocurrent method and cell performance.

- We have studied the stability of various dual-bandgap, double-junction cells in terms of the bandgaps of the bottom cells and the current mismatch between the component cells. Using a bandgap-profiled bottom cell and optimized current mismatch, we have achieved active-area (0.25 cm^2) efficiency of 11.16% as measured using a single-source simulator after 600 h one-sun 50°C illumination. **This is the highest stabilized small-area efficiency reported for a-Si alloy solar cells.** A similarly degraded cell measured under NREL dual-source simulator showed an active-area efficiency of 10.4%.

- We have made a large number of double-junction modules with aperture area larger than 900 cm^2 showing initial efficiencies exceeding 10%. The highest initial aperture-area efficiency measured indoors at USSC is 10.6%. Our light-soaking measurements indicate typically 15% to 18% degradation of these panels after 600 h one-sun exposure at 50°C.

1

Section 1

Introduction

The research program is directed toward advancing our understanding of amorphous silicon alloys and other relevant non-semiconductor materials for use in large-area multijunction modules. An important thrust of the program is on performance of modules after long-time light exposure; therefore, study of light-induced degradation forms an important part of the program. The goal of this phase of the program is to demonstrate a stable, aperture-area efficiency of 10% for a two-terminal, multi-bandgap, multijunction module of aperture area of at least 900 cm^2.

The program is divided into three tasks. Task I, semiconductor materials research, is directed toward depositing, optimizing and characterizing of suitable amorphous silicon alloy materials and cell structures over 900 cm^2. Task 2, non-semiconductor materials research, involves investigating suitable back reflectors and antireflection coatings and also encapsulants for the modules. Task 3, module research, is directed toward fabricating modules involving grid patterning, cell isolation and interconnect, and encapsulation.

In this report, we outline the progress made toward the program goal in the different task areas. In Section 2, we describe the results from optical modeling work which we have undertaken to identify optical losses in the different layers of the solar cell. In Section 3, we discuss the results of fundamental studies on materials and cells in which the intrinsic layers are deposited at different rates. We demonstrate that microstructure of the material has profound influence on cell efficiency and stability. We also investigate the stability of the component cells in a multijuntion structure and discuss an optimized cell design using a double-junction structure which gives a stable active-area (0.25 cm^2) efficiency of 11.2%. In Section 4, we discuss our large-area deposition status and report active-area (0.25 cm^2) initial efficiencies of 12% for double-junction structures. The stabilized small-area efficiency after 600 h of one-sun 50 °C degradation is 10.3%. We have made a large number of one-square-foot modules using the double-junction structure with initial aperture-area efficiencies exceeding 10%. The highest efficiency achieved is 10.6% as measured under SPIRE 240A simulator equipped with a peak detector circuit. In Section 5, we study the effect of current matching of component cells on the energy delivery from double-junction panels. Conclusions and future directions are discussed in Section 6.

Section 2

Optical Modeling

Introduction

One of the primary methods of increasing solar cell conversion efficiency is to enhance weakly absorbing, long-wavelength light. It can be shown that improving light confinement by encouraging light trapping via back reflector design can result in large increases in the amount of absorbed light.[1] At present, it is clear that our PV devices have much scope for improvement in this regard.[2] Thus, we are strongly motivated to investigate with thoroughness the optical performance of our solar cells in the hope that correctable deficiencies may be uncovered. To this end, a study of the optical losses in our devices was initiated.

Although we have a general knowledge of the optical performance of the layers comprising our solar cells, we wished to investigate the effect of parasitic optical losses in a more detailed manner. In particular, we wanted to know the absorption and thickness of each layer in our solar cells. This information can be obtained for the layers independently by making films on glass and using ellipsometry, for instance. However, we were concerned that the film growth of each layer may be affected by previous and subsequent depositions. In fact, we have experienced such phenomena occasionally in our solar cell fabrication. In addition, it would be advantageous to have a troubleshooting tool that could identify anomalous optical absorption and confirm expected film thickness.

We realized that it might be possible to glean specific optical information from standard solar cell measurements, namely spectral response and reflection. Spectral response has solid information about top-of-cell absorption, intrinsic layer absorption and intrinsic layer bandgap. Reflection measurements contain information about the thickness of the optical stack, dispersion of refractive indices, and, as will be shown, parasitic optical losses. Our laboratory is equipped with an apparatus that can measure the spectral response with colored light and (or) electrical bias.[3] Also, recently our laboratory staff had designed and built a large diameter integrating sphere that has been shown to accurately measure reflection versus light wavelength. By using spectral response and reflection measurements together, we hoped that the performance and thickness of individual layers could be extracted. This turned out to be correct.

Methodology

In this section the system for representing the film layers is described. The solar cell is represented by an optical stack that consists of homogeneous layers with sharp interfaces (Fig. 1). NIP solar cells deposited on flat substrates were used for this work, as the models assume homogeneous, specular films. The materials and film growth conditions are substantially the same as for our state-of-art multi-junction solar cells made on
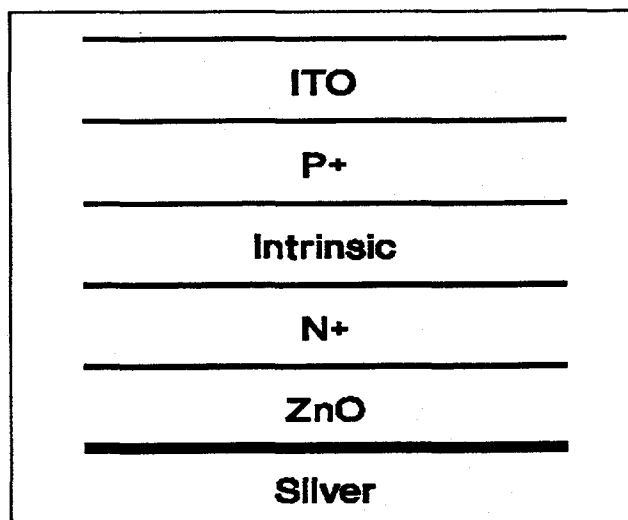
Figure 1. Structure of solar cells used in this study.

3

textured substrates. Each layer is represented by its thickness, absorption coefficient, and index of refraction. If these values are known at each wavelength, for all films in the optical stack, then reflection and spectral response curves may be calculated using coherent wave theory.[4] Light interference effects are treated realistically in this formulation. There are two requirements that are needed to connect measured data to the optical values in the stack: models for the absorption and dispersive index of each layer, and a computer algorithm to parameterize the models to the measured data (i.e., spectral response and reflection).

The absorption was modeled in the semiconductor layers to match an exponential at low energies and to match a power law at higher energies.[5] This formulation is a Tauc plot with a tail. The representative equations follow:

(1) $\alpha \equiv \exp[T*E - T*Em] * S^2 * (Em - Eg)^2 / Em$, when $E < Em$

(2) $\alpha \equiv S^2 * (E - Eg)^2 / E$, when $E > Em$

    where α is the absorption, E is the energy,

    and Eg, T, & S are parameters (Eg is the optical bandgap),

    and $Em \equiv (1 + Eg*T + [(1 + Eg*T)^2 + 4*Eg*T]^{1/2}) / 2*T$.

The indices in the semiconductor layers are represented by a Cauchy power series:

(3) $n \equiv n_0 + n_1/\lambda^2 + n_2/\lambda^4$

    where n is the index of refraction and n_0, n_1, & n_2 are parameters.

Due to absorption profiles of oxide layers measured in our laboratory, an oscillator function was chosen to represent the ITO and ZnO layers.[6] Using this theory with two oscillating energies, the following formulas were derived:

(4) $n \equiv A - [B/(w^2 + C^2)] + D*(1 - E*w^2)/[(1 - w^2*E)^2 + w^2*E^2*F^2]$

(5) $k \equiv [B*C*w/(w^4 + w^2*C^2)] + D*E*F*w/[(1 - w^2*E)^2 + w^2*E^2*F^2]$

    where n is the refractive index,

    k is the extinction coefficient, w is the oscillation frequency,

    and A, B, C, D, E, & F are parameters.

Thus each layer in the optical stack is characterized by seven adjustable parameters; the index and absorption calculation for both models have six parameters and the thickness of each layer is also required. The index and extinction coefficient for the metal substrates were measured in air. These values were used in our calculations without adjustment. A computer algorithm that could adjust these parameters simultaneously while minimizing the error of the output spectral response and reflection was chosen.[7] The average error-of-fit for the results of the subsequent sections was about 0.5%.
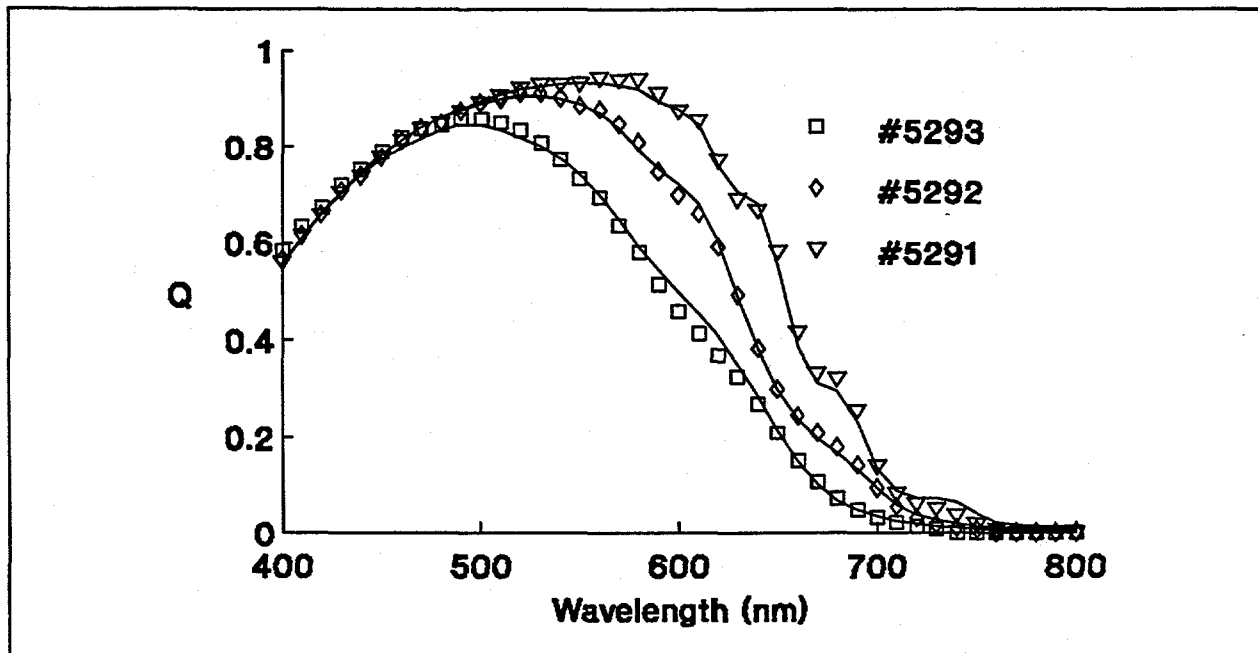
Figure 2. Measured (symbols) and calculated (lines) spectral response (Q) versus wavelength for three solar cells.

Tests of the Technique

To test this method, a series of three solar cells was fabricated. These cells differed in their structure compared to Fig. 1 in that there was no ZnO or Ag layer and the substrate metal was stainless steel. The deposition conditions were identical except that the time for deposition of the intrinsic layer was varied using a 1:2:4 ratio. The ITO layer for these cells was coated in the same deposition run. The spectral
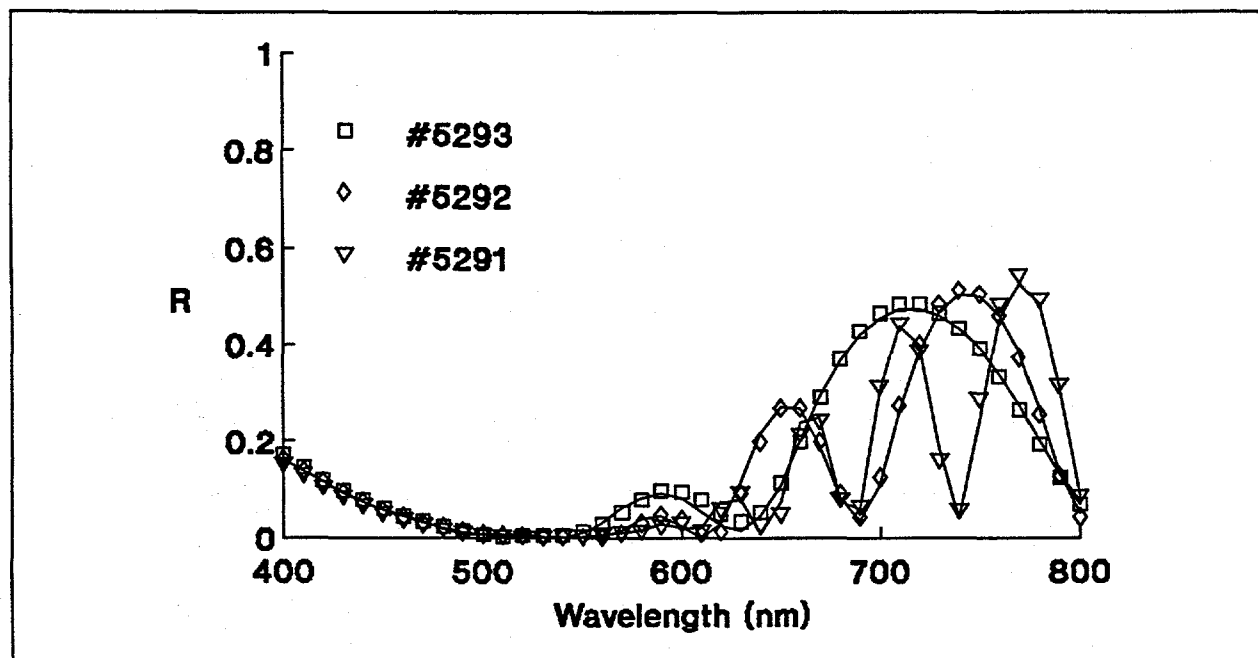
Figure 3. Measured (symbols) and calculated (lines) reflection versus wavelength for three solar cells.

response and reflection curves were measured for each cell. The spectral response was measured while electrically biasing the solar cells three volts in reverse to minimize collection effects at short circuit. The measured data was fit using the computer algorithm described previously. During the fitting process, the parameters were forced to be identical for each of the three cells except the intrinsic layer thicknesses. The results are illustrated in Figs. 2 and 3. The fitted layer thicknesses are given in the table below:

Table 1. Layer thickness from computer fit.

Layer	Thickness
ITO	66 nm
P	12 nm
I(#5291)	925 nm
I(#5292)	462 nm
I(#5293)	237 nm
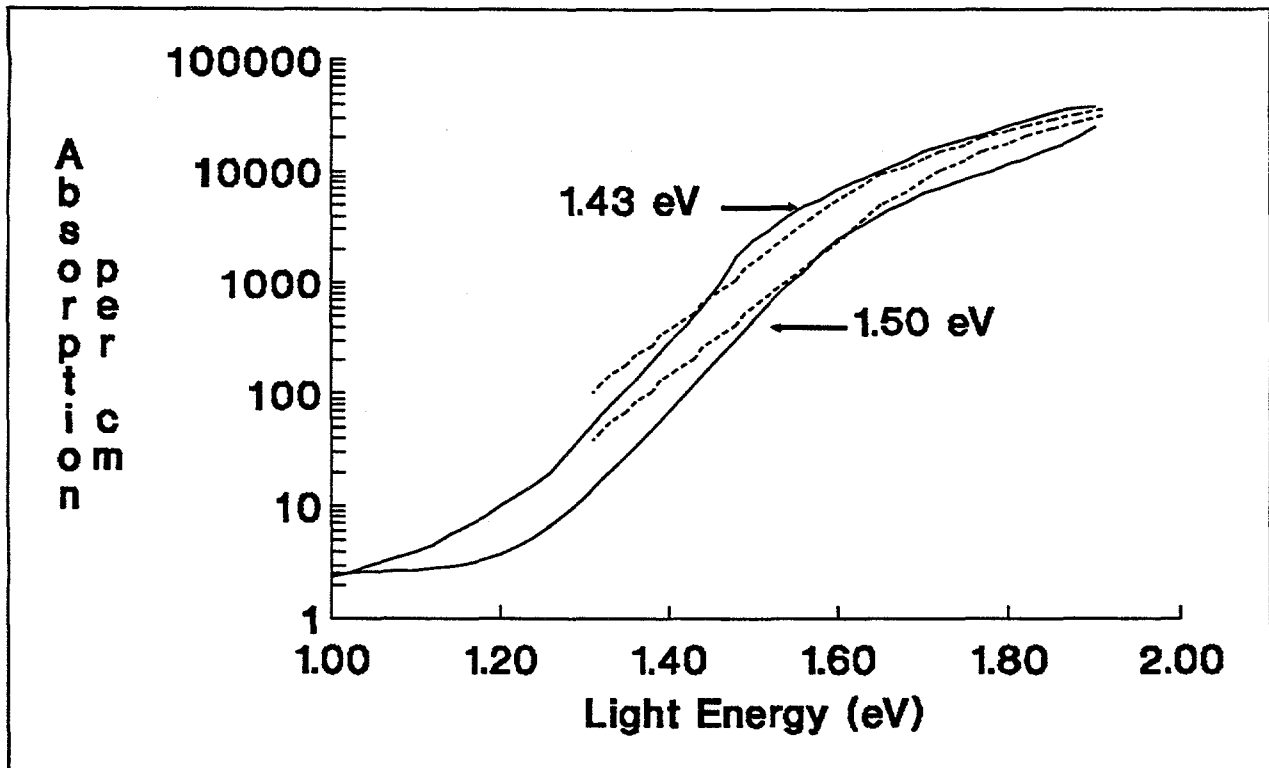
Figure 4. Calculated absorption of intrinsic layer versus light energy. The graph compares to measured (solid lines) PDS spectra. The bandgap of these cells is indicated.

It can be seen that the calculation excellently coincides with measured data in both Figs. 2 and 3. The layer thicknesses output from the calculation coincide well with expectation. Note that the ratio of intrinsic layer thicknesses due to each solar cell closely match the expected 1:2:4 ratio due to the deposition times mentioned in the above discussion. The intrinsic semiconductor model outputted a value for the optical bandgap of 1.725 eV. This agrees well with independent measurement on single films. Another indication of the accuracy of the semiconductor model is illustrated in Fig. 4. This figure displays a comparison of the absorption of two intrinsic layers with photo-thermal deflection spectra (PDS). The absorption was

6

calculated by fitting each solar cell to measured data as described above. The intrinsic layer bandgaps of these cells were engineered to have differing values by varying germanium content in the films. This figure illustrates the model's ability to extract sub-bandgap absorption. Even though the spectral response signal was very low because the substrate in this experiment was specular stainless steel (a poor reflector), reasonable values were calculated for the absorption. The calculation differs from the PDS measurement at low energies. This is probably because there is so little information from the spectral response. Spectral response measurements with higher sensitivity than those used in this work have shown this to be true.

Optical Loss Results

Figures 5 and 6 represent an optical loss study on a solar cell. Figure 5 compares a fitted cell calculation versus an additional calculation setting the absorption of the ITO and P layers equal to zero. The short circuit current values in the figure were calculated using AM1.5 Standard Global Insolation. Figure 6 compares the fitted calculation of the same cell with a new calculation setting the ZnO layer absorption equal to zero. It is interesting to notice on this drawing that while the spectral response (Q) deviates only slightly, the reflection in the long wavelength portion of the spectrum has a strong signal. We are attempting to utilize this "fingerprint" to track the cell loss as we perform experiments to identify its cause. It can be seen from the figure that this loss only represents 0.3 mA/cm^2. However, this loss causes much concern because of its implication for solar cells deposited on textured, highly reflecting substrates. In this case, a Lambertian scattering calculation reveals that such a loss could reduce the short circuit current by as much as 4.5 mA/cm^2.[8] Additional study of individual layer reflection has revealed that this loss is not present in as-deposited ZnO film. Work continues to identify the cause of this parasitic loss. The reader should be reminded that while the model formulation attributes absorption as a bulk effect, this is not necessarily so.

Conclusions

The particular merit of this work is that the actual device structures are examined as opposed to, for instance, individual film measurements on glass substrates. The measurements required for the fitting calculations are standard making the method easy to use. Analyses, such as that of Figs. 5 and 6, show which layers contribute to parasitic absorption losses and predict the enhancement in solar cell performance should these losses be mitigated against.
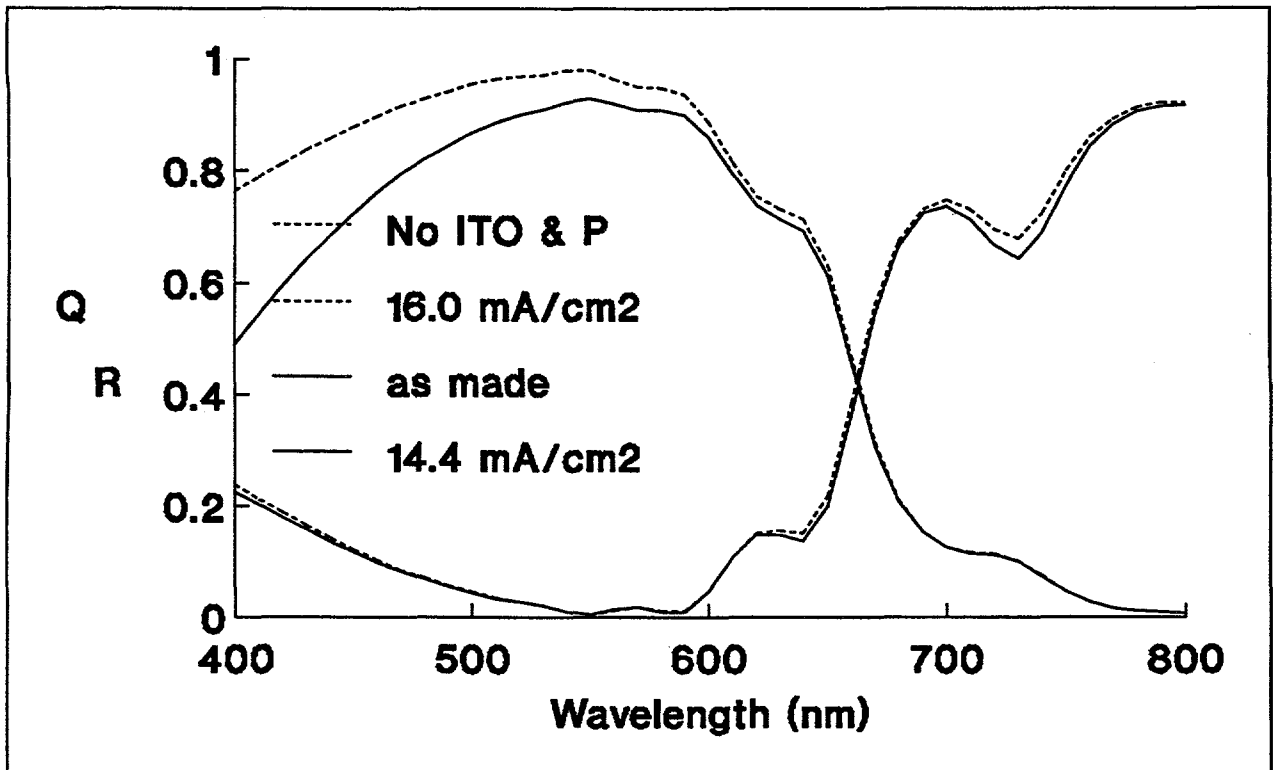
Figure 5. Spectral response and reflection of a solar cell with (solid line) and without (dotted line) ITO & P layer absorption.
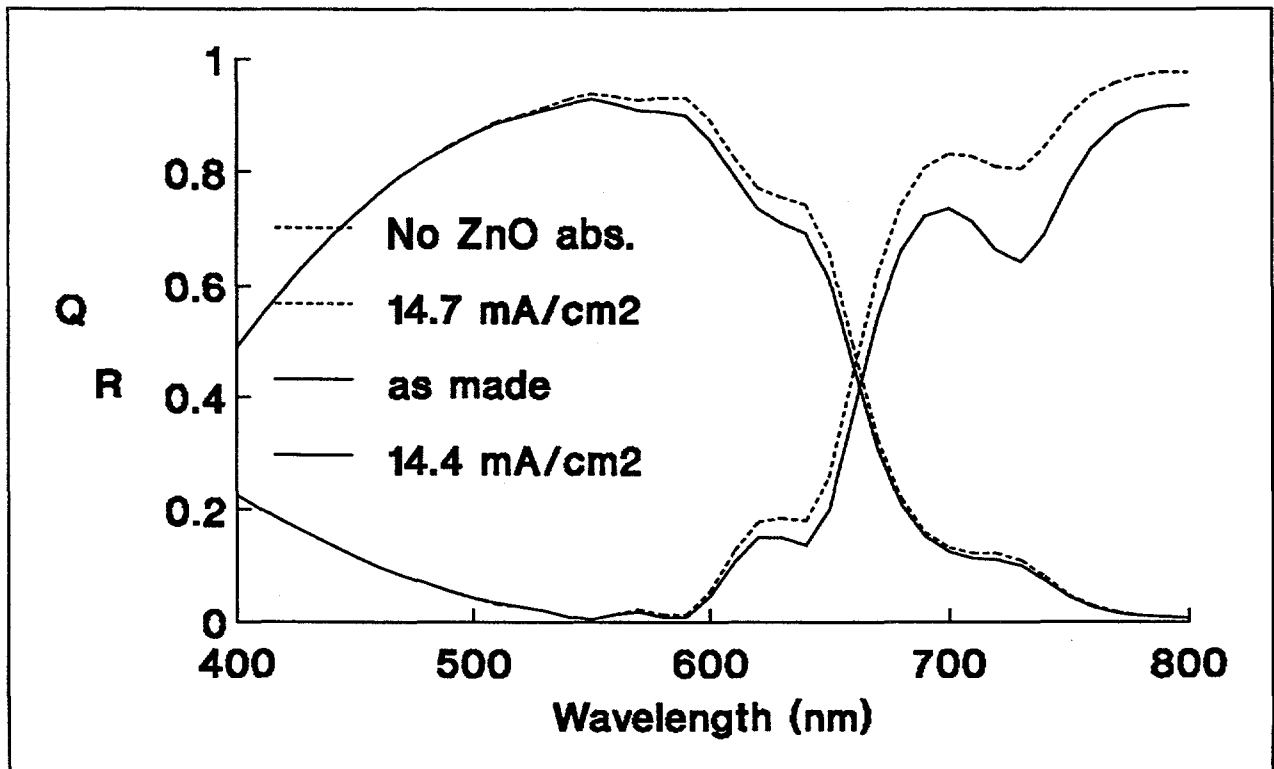
Figure 6. Calculated spectral response and reflection with (solid line) and without (dotted line) ZnO layer absorption.

Section 3

Materials and Cell Research

Introduction

In order to obtain a basic understanding of the origin of as-grown and light-induced defects in a-Si alloy films and cells, we have carried out investigations on both material properties and cell performance using materials deposited under similar conditions. The first investigation addressed the issue of correlation between microstructure of the material and cell performance where the microstructure was altered by changing the deposition rate of the intrinsic layer. Both the defect generation and annealing were investigated for one-sun and high-intensity light soaking. We also measured the defect density in amorphous silicon-germanium alloys with different germanium content and the corresponding cell performance. The aim was to determine if film measurements are adequate to predict cell performance. Finally, we investigated the light-induced degradation in component cells of a multijunction structure and also the effect of mismatch of the component cells in a double-junction structure to arrive at an optimum design for obtaining the highest stabilized efficiency.

Microvoids and Cell Performance

Light-induced degradation of hydrogenated amorphous silicon (a-Si:H) alloy materials and devices has been the subject of intensive studies.[9] It is generally agreed that recombination of excess electron-hole pairs generated by illumination creates metastable defects in the bulk of the material.[10] The defect states reduce the mobility-lifetime product of electrons and holes and causes degradation of solar cell performance. The origin of the metastability is not quite understood, and the list of causes includes[11] hydrogen, impurities like C, O, or N, microvoids due to inhomogeneous growth, weak bonds or a combination of these.

Using small-angle X-ray scattering (SAXS) measurement, it has been recently demonstrated[12,13] that even in the best quality material, microvoids of typical diameter 1.0 nm exist, occupying a volume fraction of about 1%. The void density is typically larger for poorer quality material.[14] In order to correlate the microvoid density in the material with the initial and light-degraded performance of solar cells, we have fabricated single-junction p i n solar cells in which the intrinsic layer has different microvoid density caused by changes in the deposition rate. The results are reported in this report.

Single-junction p i n solar cells were grown by the rf glow-discharge technique on stainless steel substrates kept at 300 °C. Details of deposition parameters are given elsewhere.[15] The intrinsic layer was grown using a disilane-hydrogen mixture, and the dilution of the mixture and rf power density were changed to obtain deposition rates between 0.14 and 1.35 nm/sec. The thicknesses of the i layers were kept constant at ~ 420 nm. The deposition conditions for the doped layers were kept the same for all the samples. The top contact was made using thermally evaporated indium tin oxide (ITO). Cell performance was measured under global AM1.5, red, and blue illumination.

Samples consisting of only the i layer, typically 1 μm thick, were deposited separately on crystalline silicon wafers for infrared (IR) measurements and on thin, iron-free, high-purity Al foils for SAXS measurements. The deposition conditions were nominally identical to those used to produce solar cells. Details of the SAXS experimental methods have been discussed elsewhere.[16]

Figure 7 shows the SAXS data for three samples prepared with different deposition rates where the natural log of the normalized scattering intensity[16] is plotted versus the magnitude of the scattering vector h and compared to the SAXS signal from a 70 µm crystalline Si wafer (polished on both sides). There is a clear systematic increase in the SAXS signal with increasing deposition rate. Above about 2 nm^{-1} the SAXS intensity is essentially angle independent for the 0.14 and 0.62 nm/sec deposition rates, and we believe this is due primarily to Laue monotonic scattering[17] by the Si-H alloy matrix which should increase with increasing H content. This accounts for most of the difference between the crystalline Si and the two lower deposition rate a-Si:H films above h=2 nm^{-1}. The film grown with the highest rate clearly shows angular dependence in the SAXS up to the largest angles. After correcting for the angle-independent contribution for all three samples, we estimate the volume fraction of voids (V_f) assuming a simple two-phase system (voids and matrix) as described in detail elsewhere.[14,16] We find similar values of V_f of 1 ± 0.5% for the samples prepared with 0.14 and 0.62 nm/sec deposition rates and 4 ± 1% for the one deposited with the 1.35 nm/sec rate.

In order to explore the shape and orientation characteristics of the voids, the sample with the largest void-fraction was measured at a tilt angle of 45°, and the results are compared to the non-tilted data in Fig. 8. The data are identical within experimental error, and this demonstrates that the voids are of spherical shape or, if non-spherical, randomly oriented throughout the sample.[14]

The sample with the large void fraction was also analyzed to extract the approximate void size distribution by fitting a superposition of SAXS curves due to a few distinct spherical microvoid diameters and adjusting the sizes and volume fractions to give a good fit. We estimate that about 80% of the void volume is due to diameters of 0.9 nm with most of the remainder less than 10 nm in diameter. The very small voids account for most of the increase in V_f compared to the two films prepared at the lower deposition rates.

The initial and light-degraded (after 600 h one-sun, 50 °C, open-circuit condition illumination) performances of the solar cells as a function of i layer deposition rate are shown in Fig. 9. The initial efficiency is found to decrease above deposition rates of ~ 0.35 nm/sec. The light-degraded efficiency shows a systematic, continuous decrease as the deposition rate is increased. It is interesting to note that at a deposition rate of 0.14 nm/sec, the relative degradation is only 12.5% whereas at 1.35 nm/sec, the relative degradation is 43%. We should mention that since the samples are deposited on stainless steel, both the initial and final efficiencies are lower than those on an optimized back reflector. A reference cell of the same thickness deposited on Ag/ZnO back reflector at a deposition rate of 0.14 nm/sec has an initial efficiency of 11% and degrades by about 30% under the same light-soaking condition. Since photon absorption is enhanced with a back reflector, the generation rate of carriers is larger, and this results in a higher degradation.

Since increasing deposition rate leads to higher void density, the results indicate an enhancement in degradation of solar cells with the i layers having more microstructure. This is consistent with earlier results[18] which showed an increase in light-induced sub-bandgap absorption in films that showed more microstructure as determined by the ratio of infrared absorption at wave numbers 2070 cm^{-1} and 2000 cm^{-1}. For our films deposited at 0.14 nm/sec, the hydrogen content is 8% whereas that for the deposition rate of 1.35 nm/sec is 12%. The ratio of the microstructure fraction, R, as defined by R = $I_H(2070)/[I_H(2000)$ + $I_H(2070)]$ increases from 8.4% to 18.4% in these two films. $I_H(2000)$ and $I_H(2070)$ are the integrated infrared absorption due to the stretching mode bonds at 2000 cm^{-1} and 2070 cm^{-1}, respectively.[19] It should be pointed out that although R increases from 8.4% to 18.4% as the deposition rate is raised from 0.14 nm/sec to 1.35 nm/sec, C_H (2000), which is the concentration of hydrogen bonded in the Si-H monohydride mode at 2000 cm^{-1}, remains constant at around 6.4%. This suggests that, at least in these

10
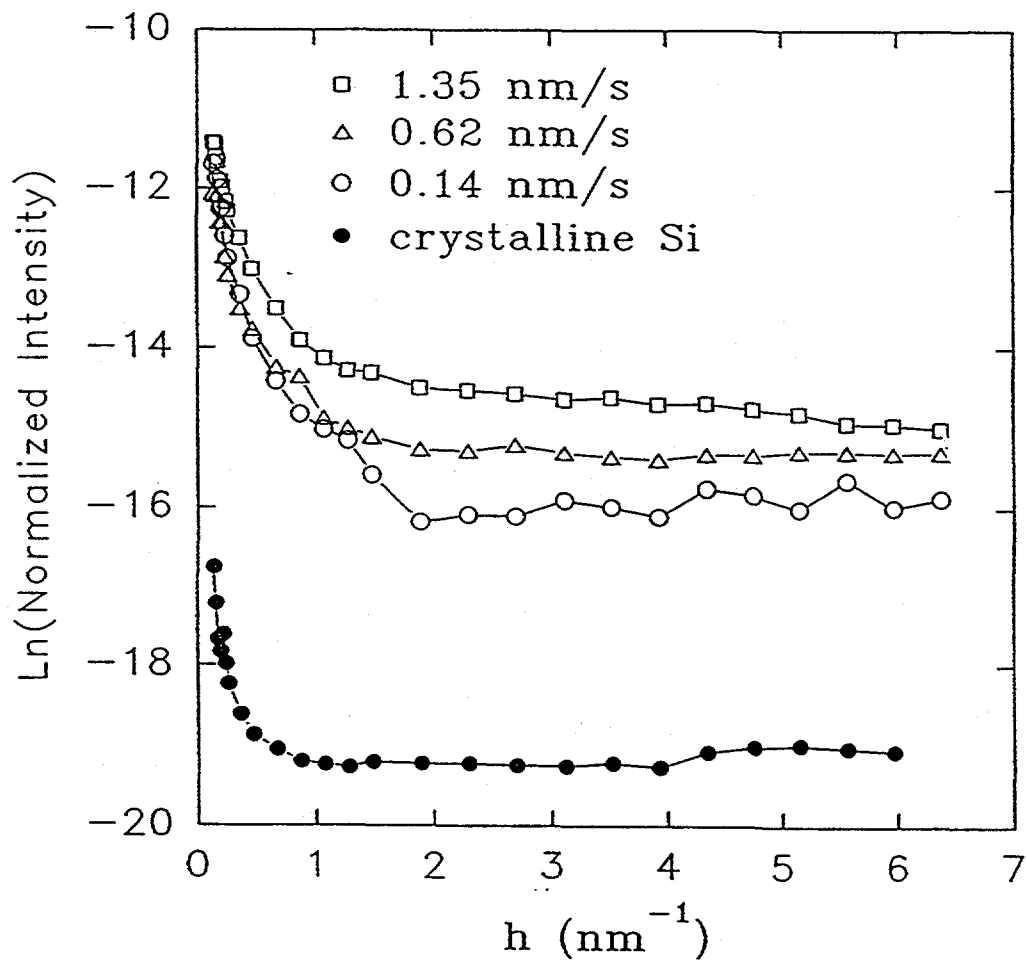
Figure 7. SAXS data for a-Si alloy films grown at different deposition rates compared to data from a crystalline Si wafer. The intensity has been normalized and corrected for substrate effects according to the procedure in ref. 16. $h=4\pi\sin\theta/\lambda$, where $\lambda=0.154$ nm and 2θ is the scattering angle. The solid lines are drawn to connect the data points.
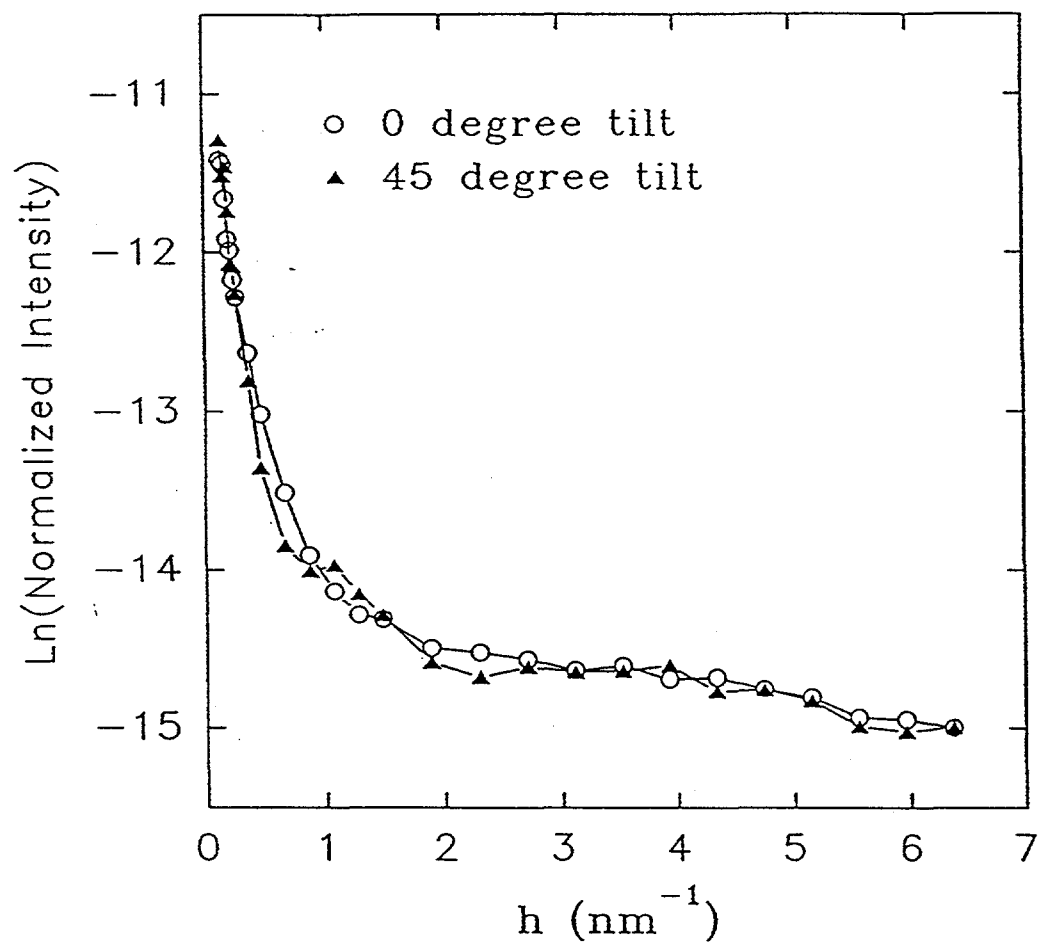
Figure 8. SAXS data from the sample grown at 1.35 nm/sec mounted in two orientations relative to the X-ray beam.
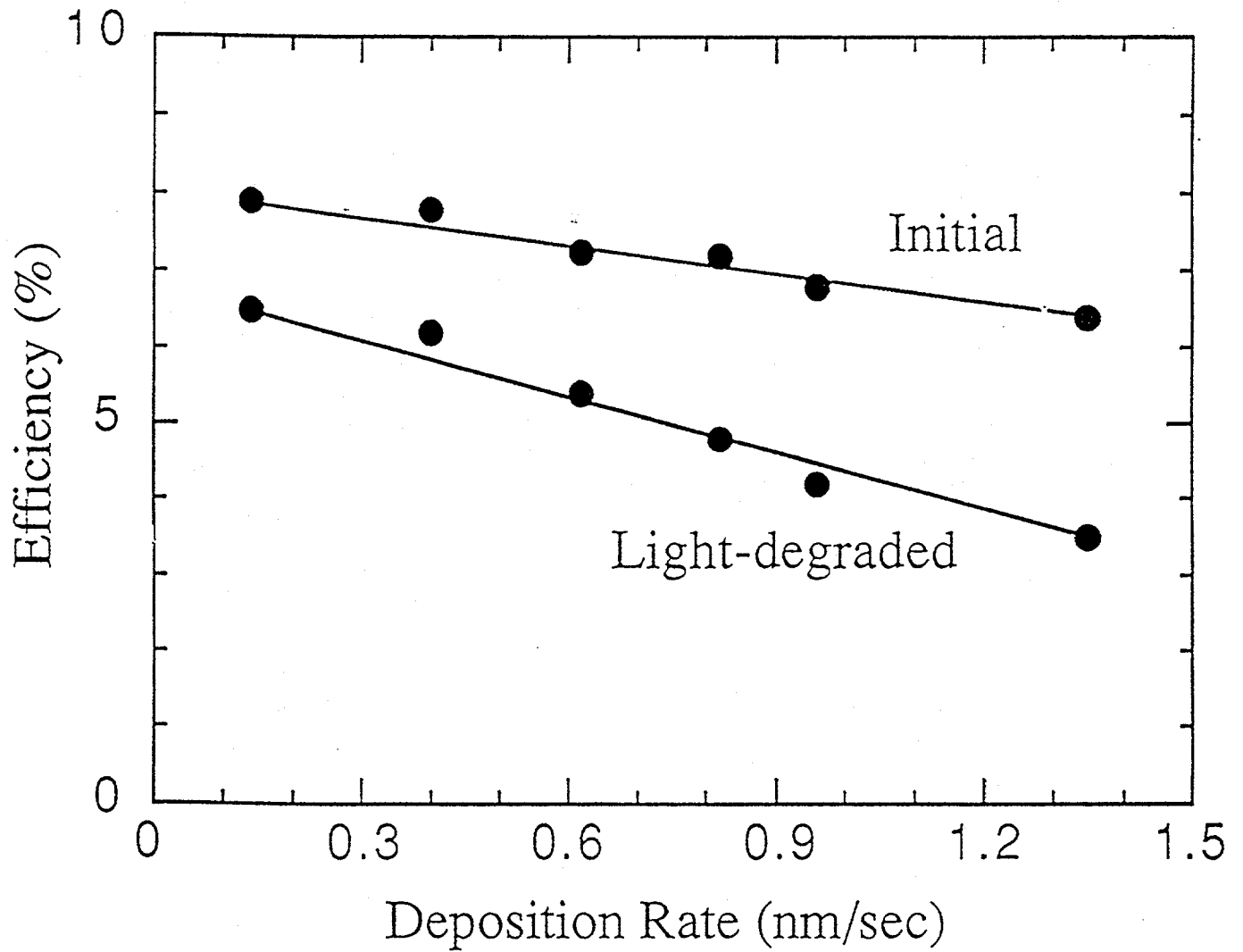
Figure 9. Initial and light-degraded efficiencies of a-Si alloy solar cells as a function of deposition rate.

films, the degradation process is not associated with the isolated Si-H bonds in the dense amorphous matrix. It also suggests that the increased angle-independent SAXS contribution with increasing deposition rate (proposed above to be the Laue monotonic scattering from increased H in the a-Si:H matrix) is not due to increased numbers of isolated Si-H bonds but rather to bonds associated with the 2070 cm^{-1} mode.

Our results, showing increased light-degradation in materials with larger void-fraction and microstructure fraction, do not support the suggestion by Matsuda et al.[20] that material with increased microstructure may be more stable. Their conclusion was based on photoconductivity measurements on materials deposited from Xe-diluted silane mixtures. The dangling bond density, both in the initial and light-degraded state, was, however, found to be higher for films with poorer microstructure. As we shall discuss below, this is in agreement with our solar cell results.

We should mention that our results show a decrease both in the initial and degraded performance of the solar cells with increase in the density of microvoids whereas the results of Bhattacharya and Mahan[18] showed no change in the initial quality of the film as determined by sub-bandgap absorption even when R was as high as 50%. The sensitivity in measurement of solar cell efficiency, of course, is much better than that in defect density estimation from sub-bandgap absorption. The deterioration of the material quality as a function of increased microstructure is evident from Table 2 where we have tabulated results from both microstructure and solar cell measurements for samples prepared at a deposition rate of 0.14 nm/sec and 1.35 nm/sec. The fill factor under red and blue illumination is determined by the collection length of the photo-generated carriers which, in turn, is governed by the defect density. A clear correlation between both initial and light-degraded defect density and void density is apparent. Since dangling bonds are the predominant defect centers in a-Si:H films, these results are in agreement with those reported in Ref. 20. We would like to point out that although we see a correlation between deposition rate and void density, these results should be considered only to depict the trend under certain deposition parameters. With different gas mixtures or at a different substrate temperature, it may be possible to get a lower void density even at a higher deposition rate.

In conclusion, by a combination of IR and SAXS measurements on films and efficiency measurements of solar cells, we see a correlation between microstructure and solar cell performance. With increasing microvoid density and microstructure fraction, both the initial and light-degraded solar cell performance are found to deteriorate.

Table 2. **Material Properties and Cell Performance for Samples Prepared at Two Different Deposition Rates.**

Deposition rate	0.14 nm/sec	1.35 nm/sec
Void fraction	1%	4%
Predominant void diameter	-	0.9 nm
Hydrogen content	8%	12%
Microstructure fraction (R)	8.4%	18.4%
C_H (2000)	6.4%	6.3%
Initial efficiency	7.85%	6.31%
Degraded efficiency	6.53%	3.5%
Initial red fill factor	0.67	0.52
Degraded red fill factor	0.52	0.43
Initial blue fill factor	0.73	0.67
Degraded blue fill factor	0.67	0.40

Annealing Behavior of the Metastable Defects

Since microstructure plays an important role in determining both the as-grown and the metastable defect densities, it is interesting to find out if it influences the annealing behavior of the defects as well. Table 3 shows the recovery of the cells reported earlier after annealing at 150°C for 90 minutes. η_I is the initial efficiency, η_D is the efficiency after one-sun light soaking for 600 h at 50°C and η_A is the efficiency after subsequent annealing at 150 °C for 90 minutes. It is interesting to note that as the deposition rate increases, the recovery is slower as if there are some defects which are harder to anneal. After prolonged heating at 190°C for 10 hours, the cell efficiencies could be restored to their initial values.

There have been several reports describing different annealing behaviors of metastable defects in materials prepared or illuminated under different conditions. It has been reported that metastable defects in B-doped a-Si alloys are easier to anneal.[21] Addition of impurities like O, N, or C in quantities in excess of 1% also affect the annealing kinetics of the metastable defects.[22] Even in undoped material, the annealing behavior of the defects is governed by the conditions under which the defects are created. Defects created under light exposures at higher temperature[23] or for longer time[24] are known to be more difficult to anneal out. This is, however, the first evidence that defect annealing is related to microstructure of the material. If annealing of the metastable defects is related to hydrogen transport, one would expect the hydrogen diffusion constant to be smaller for the structure with more microvoids. It is possible that the microvoids act as trapping sites for the hydrogen thus slowing down its motion. Another way of explaining the dependence of annealing behavior on microvoids is by assuming larger energy barriers between the stable and the metastable configurations with increasing microstructure. Further experiments will be necessary to understand this annealing behavior.

Table 3. **Annealing Behavior of One-sun Light-degraded Efficiency for Cells with Different *i* layer Deposition Rates.**

Deposition Rate (nm/s)	0.14	0.35	0.62	1.35
η_I	7.78%	7.80%	7.29%	6.31%
η_D	6.81%	6.47%	5.49%	3.58%
η_D/η_I	87.5%	82.9%	75.3%	56.7%
η_A	7.42%	7.20%	6.18%	4.93%
η_A/η_I	95.4%	92.3%	84.8%	78.1%

Accelerated Degradation

High intensity light soaking is being extensively used by several laboratories to predict saturation behavior of light-induced degradation in a-Si alloy materials and devices. In order to determine that the observed saturation after high intensity illumination does reflect the degradation under one-sun condition, it is important to establish that the defects created at different illumination intensities are similar. We have done some experiments to investigate this problem, and the results are presented below.

In Fig. 10 we show the degradation behavior for 30-sun 48 °C light soaking on cells in which the *i* layers were deposited at two different rates (0.14 and 1.35 nm/sec). The cell deposited at the lower rate shows saturation after 40 minutes. The cell deposited at the higher rate, however, degrades much more and does not show saturation even after 6.5 hours of intense light soaking, which is approximately equivalent to 6000 hours of one-sun soaking. Since the high deposition rate gives rise to larger microvoid density, these results therefore indicate that in materials with large density of microvoids, the metastable defects are more numerous. This is consistent with the conclusions based on our degradation study under one-sun illumination.

In order to see whether accelerated light soaking creates the same defects as those created by one-sun light soaking, we studied the behavior of the above cells under one-sun soaking after different periods of accelerated light soaking. The cells were first degraded under 30 suns for 0.5, 1, 5 and 30 minutes, respectively, and then further degraded under one-sun light soaking. If both accelerated and one-sun light soaking create the same defects, we expect that those devices which have already been degraded by accelerated soaking close to the saturated values under one-sun soaking will reach saturation very quickly. It is surprising that under one-sun soaking none of these devices reach saturation in a short time. As presented in Figs. 11 (a) and (b), most of these devices first show certain recovery under one-sun soaking until they reach maxima, and after that they all show degradation again. The observed recovery cannot be explained if the defects generated at 30 suns are the same as those created under one-sun condition.

Further evidence demonstrating the different nature of the defects created under one-sun and 30-sun conditions comes from thermal recovery experiments on degraded cells. In Table 4, we present experimental data on thermal recovery of cells deposited at four different rates and degraded under one-sun condition for 600 h at 50 °C. As we have shown earlier, the degradation is more as the deposition rate increases. After annealing at 150 °C for 90 minutes, the cell deposited at 0.14 nm/sec recovers to 96% of its initial value, whereas that deposited at 1.35 nm/sec recovers to only 80%. The cells were next fully annealed and again degraded with 30 suns at 48 °C to values corresponding to those for one-sun 600 h 50 °C condition. The recovery after the same thermal annealing is much larger. The low deposition rate sample is fully recovered whereas the cell deposited at 1.35 nm/sec recovers to 89% of its initial value.

These results show that accelerated light soaking generates defects which are easier to anneal out, and one cannot, therefore, get a precise understanding of cell degradation and saturation to be expected under one-sun light soaking by carrying out accelerated light-soaking experiments.
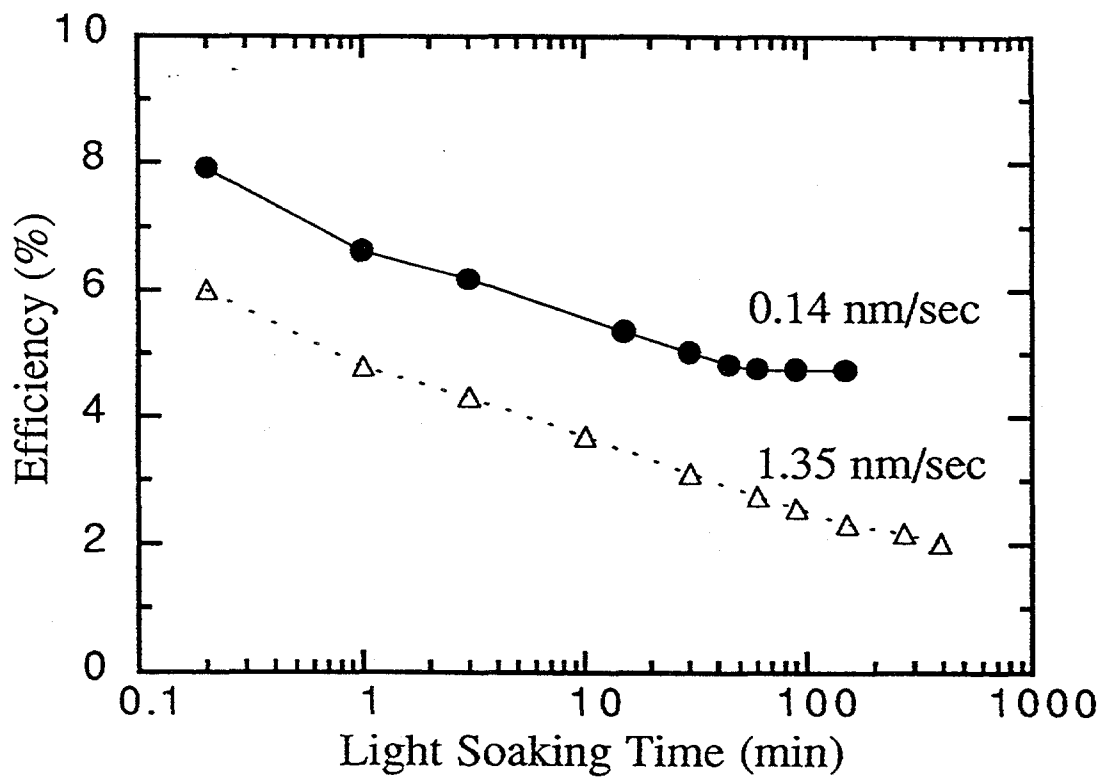
Figure 10. Efficiency as a function of 30-sun light soaking time for the cells deposited at 0.14 nm/sec and 1.35 nm/sec.

18

(a)

(b)
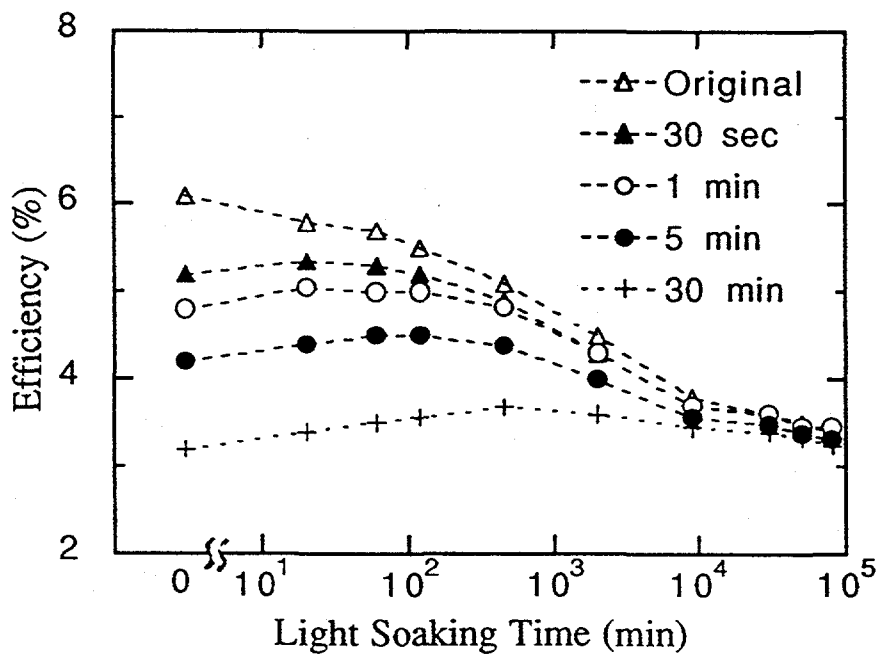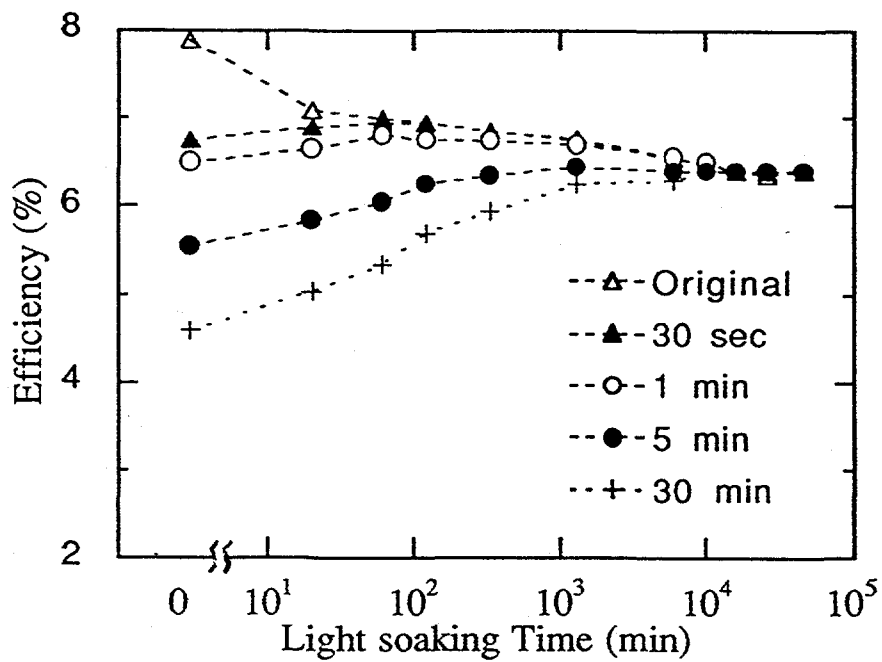
Figure 11. Efficiency as a function of one-sun light soaking time after different periods of accelerated light soaking for the cells deposited at (a) 0.14 nm/sec and (b) 1.35 nm/sec.

Table 4. **Annealing Behavior of One-sun and 30-sun Light-degraded Efficiency for Cells with Different _I_ layer Deposition Rates.** D1 designates the degradation under one-sun 600 h 50 °C condition and A1 the subsequent recovery after 150 °C 90-minute annealing. D2 represents 30-sun degradation and A2 the subsequent recovery.

Deposition Rate (nm/s)	0.14	0.35	0.62	1.35
η_i	7.78%	7.80%	7.29%	6.31%
η_{D1}/η_i	84.0%	79.2%	71.1%	53.2%
η_{A1}/η_i	96.1%	93.3%	88.8%	79.9%
η_{D2}/η_i	83.9%	78.2%	70.1%	53.6%
η_{A2}/η_i	100%	98.4%	99.5%	89.4%

Correlation Between Film Property and Cell Performance

It is generally agreed that the degradation in efficiency of solar cells is predominantly caused by deterioration of the material quality. A great deal of effort, therefore, has been made to investigate material property before and after light-induced degradation to obtain the best material for optimized solar cell performance.

The most commonly used techniques to evaluate material properties are the measurement of photoconductivity and sub-bandgap absorption. Using uniformly absorbing monochromatic light to measure the photocurrent, one can obtain the majority carrier $\mu\tau$ product in the material. Measurement of sub-bandgap absorption by photothermal deflection spectroscopy (PDS) or by constant photocurrent method (CPM) gives information about the valence band tail and the near mid-gap deep states. Integration of the sub-bandgap absorption can be correlated to the spin density in the material[25] and has been used to predict solar cell performance.[26]

The applicability of the use of defect density obtained from CPM to predict the solar cell performance, however, merits careful scrutiny. It is widely recognized[27] that the accuracy of the defect density obtained from sub-bandgap absorption measurement depends critically on several factors such as the precision of matching the sub-bandgap CPM or PDS data to absorption values measured at higher than bandgap energy and also on the accuracy of determining the slope of Urbach edge. An uncertainty of a factor of 2 to 3 in the estimated value is easily expected. A change in the defect density by a factor of 2, however, will drastically affect the solar cell performance.

In order to determine the degree of correlation that exists between material properties and solar cell performance, we have studied the material properties of a-SiGe alloy films and also the performance of cells with the intrinsic layers deposited under nominally identical conditions. The results are reported in this report.

a-SiGe alloy films, typically 1 μm thick, were deposited on crystalline silicon wafer and 7059 glass substrates from a dilute mixture of disilane and germane.[28] The germane flow was varied to obtain films with three different bandgaps. Single-junction n i p solar cells were made on stainless steel with predeposited textured Ag/ZnO back reflector. The intrinsic layers of the cells, typically 3000 Å thick, were grown under conditions nominally identical to those for the films deposited on glass.

The films on glass substrates were characterized by measurement of dark and photoconductivity, above-bandgap optical absorption and reflection and sub-bandgap absorption by photothermal deflection spectroscopy and constant photocurrent method. Infrared absorption measurement was used to determine the hydrogen content of the films deposited on silicon wafers. The solar cell performance was measured under global AM1.5 illumination and also under red and blue illumination. In Table 5 we show the properties of three films with different germanium contents. The mobility-lifetime ($\mu\tau$) product for electrons is measured with 750 nm light of an incident flux of 5×10^{14} cm^{-2} sec^{-1}. The Urbach edge (E_u) was obtained from PDS measurement, and the defect density is calculated from integrated sub-bandgap absorption below the Urbach edge as measured by CPM. We notice that the Urbach edge remains constant with increasing Ge-content; the $\mu\tau$ product, however, decreases with increasing Ge-content. The defect density for the three samples is in the range from 3.1 to 5.6×10^{15}/cm^3. Also shown in Table 5 are the properties after one-sun light soaking at 50°C for 600 h. The $\mu\tau$-products decrease for all the three samples as a result of the light soaking. The defect density increases by about a factor of 2 for the films with lesser Ge-content. For the film with 41% Ge, however, the defect density remains unchanged from the as-deposited condition.

21

Table 5. **Properties of a-SiGe Alloys with different Ge Content.**

Sample	Ge-Content (%)	Optical Gap (eV)	Eu (meV)	$\mu\tau$ $(cm^2V^{-1}S^{-1})$		Defect Density (cm^{-3})	
				Init.	Degraded	Init.	Degraded
4827	19	1.55	51	8×10^{-7}	2.7×10^{-7}	5.1×10^{15}	1.2×10^{16}
4830	30	1.50	52	3×10^{-7}	1.5×10^{-7}	3.1×10^{15}	6.6×10^{15}
4829	41	1.41	49	1×10^{-7}	4.0×10^{-8}	5.6×10^{15}	6.5×10^{15}

In Fig. 12 we show the initial and light-degraded efficiencies of cells where the i-layers are about 3000 Å thick and have been grown under nominally identical conditions to those for the films shown in Table 5. All the cells show typical light-induced degradation between 30% to 40%. In Table 6, we tabulate the performance of the cells under global AM1.5, blue and red illumination. We notice that the maximum degradation is in the fill factor of the cells. For the cell with the largest bandgap, the blue fill factor remains unchanged, whereas the red fill factor degrades by a small amount. For the cells with lower bandgap, both the red and the blue fill factors show larger degradation. The fill factor of a solar cell is essentially governed by the ease with which the photogenerated carriers can be collected at the electrodes. For the highly absorbing blue photons, the fill factor is determined by the electron transport, whereas for the more uniformly absorbing red photons, the carrier with the poorer transport property will determine the fill factor. For example,[29] in high quality a-Si alloy single-junction cells, the blue fill factor is much better than the red fill factor because the $\mu\tau$ product for electrons is much higher than that for the holes. It is interesting to note that for all the three a-SiGe alloy cells shown in Table 6, the red and the blue fill factors are very similar in the undegraded state even though the $\mu\tau$ product for electrons drops down drastically with increasing Ge-content. What is more interesting is the fact that even though the defect density as measured by CPM hardly changes after light soaking in the lowest bandgap alloy, the corresponding cell shows a large degradation in both the red and the blue fill factors. We should also point out the lack of correlation between the $\mu\tau$ value and the defect density in the a-SiGe alloys. This is partly due to the fact that even if the defect density remains the same, with increasing Ge-content, the electron mobility decreases, which would cause the $\mu\tau$ product to be lower.[30] It is interesting, however, that for the lowest bandgap alloy, even though the $\mu\tau$ product degrades after light soaking, the defect density does not change much. The dark conductivity of the sample is about the same in the degraded and the annealed states, and a shift in the Fermi level cannot explain this anomaly. As we have pointed out earlier, there can easily be an error by a factor of 2 in the estimate of defect density of different samples. On the same sample, however, the accuracy is much better. There must be, therefore, other changes taking place after light soaking which affect the solar cell performance, but cannot be detected by CPM. New states may be created above the Fermi level; the capture cross-section of the light-induced states also could be different. CPM would be insensitive to these changes.
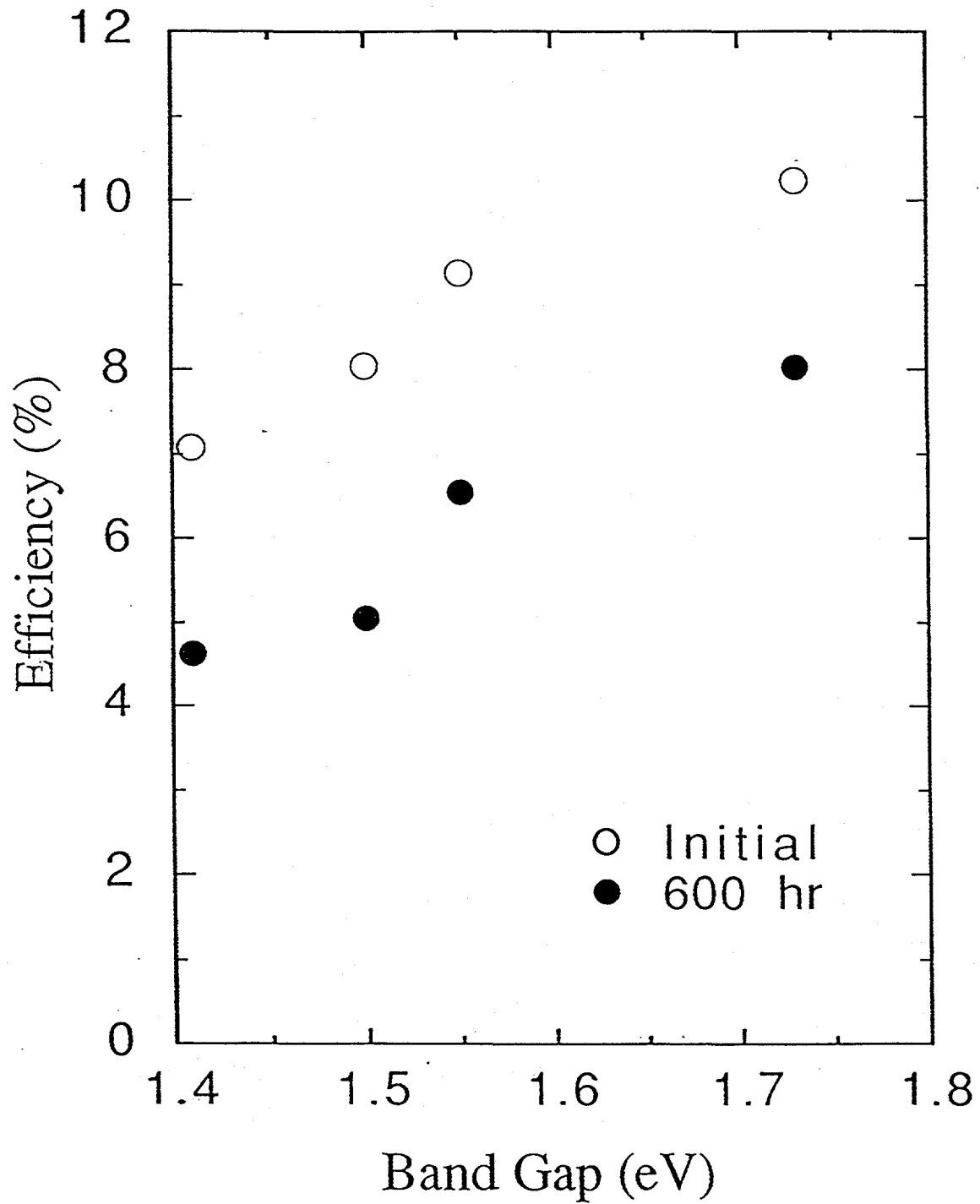
Figure 12. Initial and light-degraded efficiencies of single-junction solar cells as a function of bandgap of the intrinsic layer.

Table 6.   Performance of Single-junction a-SiGe Alloy Solar Cells before and after Light Soaking for 600 Hours under One-sun Illumination at 50 °C.

| i-layer Bandgap | State | AM1.5 Performance | | | | Fill Factor | |
		J_{sc} (mA/cm²)	V_{oc} (V)	FF	η (%)	Blue	Red
1.55 eV	Initial	18.50	0.80	0.62	9.18	0.60	0.59
	Degraded	17.21	0.76	0.50	6.54	0.59	0.54
1.50 eV	Initial	20.93	0.70	0.55	8.06	0.58	0.60
	Degraded	17.81	0.66	0.43	5.05	0.48	0.46
1.41 eV	Initial	22.39	0.61	0.52	7.10	0.60	0.59
	Degraded	19.92	0.57	0.40	4.54	0.49	0.48

We would like to emphasize that the observed lack of correlation does not imply that measurement of film property cannot give general ideas about the solar cell performance. If the $\mu\tau$ product is very low or the defect density very high, the solar cell will also perform poorly. However, with the current accuracy of CPM measurements, it is not possible to distinguish between high-quality materials where the defect densities differ by a factor of 2 or less. Moreover, as discussed earlier, factors other than the density of deep states also affect solar cell performance.

In conclusion, we have studied the performance of a-SiGe alloy single-junction solar cells both before and after light soaking. The intrinsic layers of the cells have different Ge-contents. a-SiGe alloy films were grown on glass with parameters nominally identical to those for the cells, and the film properties were measured. We do not find good correlation between cell performance and film properties for these high-quality materials.

Stability of Component Cells in Multijunction Structure

The stabilized efficiency of a multijunction cell is determined by the light-induced degradation of the component cells. Depending on the cell thickness and the germanium content, the different component cells degrade by different amounts, and a careful matching of the degraded cells is necessary to obtain the highest efficiency in the multijunction structure. We have therefore carried out light-induced degradation studies of the component cells in double- and triple-junction structures, and the results are reported below.

The component cells were made using deposition parameters that have been used in our laboratory for obtaining high efficiency double- and triple-junction cells. Both the bottom and the middle cells in this study used a-SiGe alloys for the intrinsic layers. The top and the middle cells were deposited on substrates without any back reflector, because in the multijunction configuration, these cells do not see much reflected light. The bottom cells were deposited on Ag/ZnO back reflector. The characteristics of the component cells in the initial state are listed in Table 7. For both cell measurement and degradation, the top cells were exposed to white light, while the middle and the bottom cells were illuminated with filtered light using 530 nm and 610 nm cut-on filters, respectively. The temperature during degradation was kept at 50 °C.

Table 7. **Characteristics of the Component Cells in the Initial State.** The top cells are measured under global AM1.5 illumination, the middle cell with global AM1.5 and a 530 nm cut-on filter and the bottom cell with global AM1.5 and a 610 nm cut-on filter.

Sample No.	Designation	P_{max} (mW/cm^2)	J_{sc} (mA/cm^2)	V_{oc} (V)	FF
5344	Top/double	6.84	10.30	0.94	0.71
5342	Top/triple	4.39	6.50	0.94	0.72
5343	Middle/triple	3.51	7.02	0.77	0.65
5346	Bottom/double	4.16	9.80	0.68	0.63
5345	Bottom/triple	3.65	8.59	0.68	0.63

As shown in Figs. 13 and 14, the top and the middle cells reach saturation in degradation before 600 hours, and the bottom cells show a tendency of saturation around 600 hours. In a separate experiment, we have seen saturation in degradation in the bottom cell under one-sun illumination after 1000 hours. For component cells in the double-junction devices, the top cells degrade by 12%, and the bottom cells degrade by 18% (Fig. 13). In the triple-junction case, the top cells degrade by about 11%, the middle and the bottom cells degrade by about 16%-18% (Fig. 14). Based on the data obtained from these component cells, one can predict that the double-junction cells will degrade between 12%-18%, and the triple-junction cells will degrade by 11%-18%.
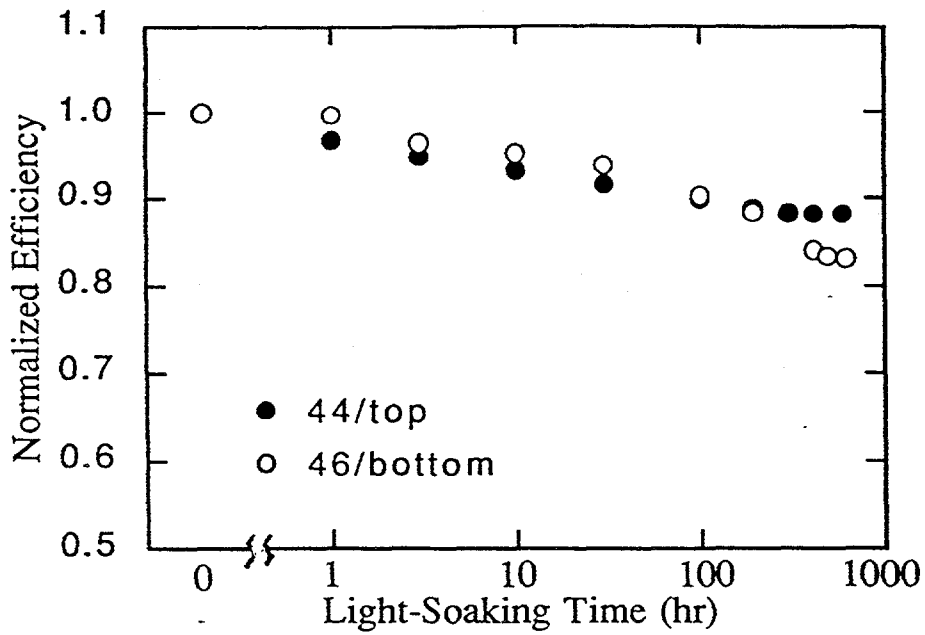
Figure 13. Normalized efficiency of the top and bottom cells for the double-junction configuration as a function of light-soaking time.
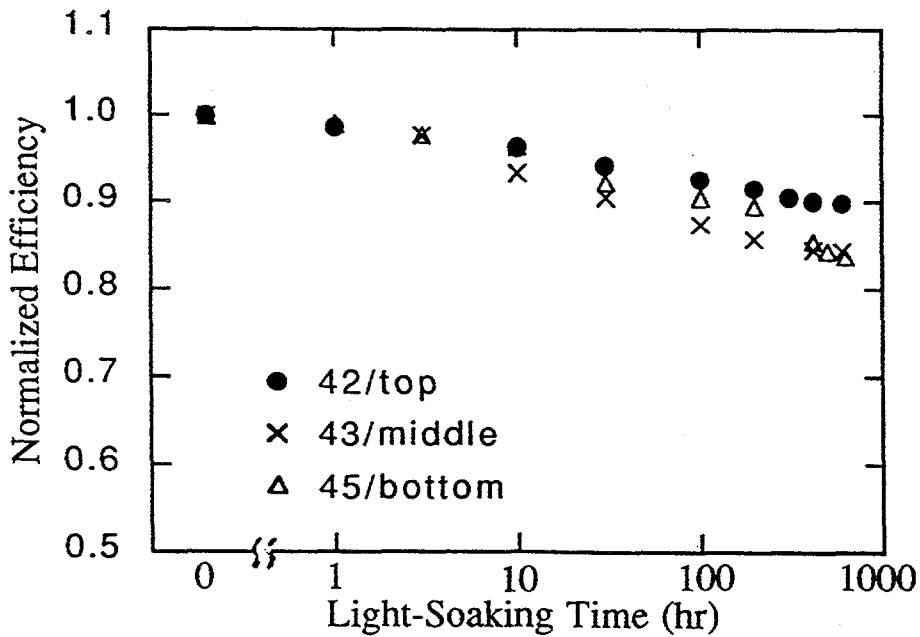
Figure 14. Normalized efficiency of the component cells for the triple-junction configuration as a function of light-soaking time.

26

One surprising result is that the top cells, although very thin, degrade by 10%-12%, of which the degradation in V_{oc} is about 5%. Note that the V_{oc} of thin top cells in this work is 0.94 V. Obviously, reducing the degradation of V_{oc} of top cells can improve multijunction solar cell stability. Accelerated degradation experiments (30 suns, 48 °C, 5 minutes) were done on several cells with the i layer deposited with different deposition rate (0.15 nm/sec and 0.8 nm/sec) or with different interface layer between p and i layers, i.e., low-rate i layer with high-rate "buffer," or high-rate i layer with low-rate "buffer." In all cases, 50-60 mV degradations in V_{oc} were observed. More experiments are in progress to study the degradation in V_{oc}.

We have also assessed the applicability of using a-Si alloy for the intrinsic layer of the middle cell in the triple-junction configuration. From the stability study of the middle cells with different thicknesses, we found that under no case could the middle cells produce more than 7 mA/cm² of current density (under > 530 nm filter) in the degraded state. In order to obtain stable high-efficiency, triple-junction cells, the middle cell must provide a minimum of 7 mA/cm² in the degraded condition, and one must therefore incorporate Ge in the middle cell to obtain high stabilized efficiency.

Since the top cells have the highest fill factor and the least degradation in the saturated state, the current of each component cell in the multijunction cells should be adjusted to be top-cell limited. As we shall describe later, using this procedure, we have achieved an 11.2% stabilized active-area conversion efficiency for dual-bandgap, double-junction a-Si alloy solar cell.

Stability Study on Double-junction Cells

We have previously reported[31] that initial conversion efficiencies of $\geq 13\%$ can be achieved in amorphous silicon-based multijunction solar cells. Here we report the results of our stability study on various dual-bandgap, double-junction devices in which the top and bottom cells were made from hydrogenated amorphous silicon (a-Si:H) and hydrogenated amorphous silicon-germanium (a-SiGe:H) alloys, respectively.

To obtain a high-performance, double-junction cell, the component cells should have high efficiency and stability. However, the quality of the narrow bandgap a-SiGe:H material is usually poorer than that of a-Si:H. One can get better results by mismatching the cells so that the limiting cell is the a-Si:H cell, which has a better fill factor.

We have fabricated various double-junction 0.25 cm² devices in which the bottom a-SiGe:H cells have bandgaps ranging from 1.41 to 1.55 eV. We have studied the effect of bandgap variation and current-mismatching on the stability of the double-junction devices. Most of the devices investigated stabilized at an active-area efficiency of about 10% while the best performance was obtained from incorporating a profiled bandgap in the bottom cell having a bandgap of 1.41 eV at the narrowest region. A stabilized active-area efficiency of 11.16% was observed after 600 hours of one-sun illumination at 50 °C. This is believed to be the highest stabilized value reported to date on amorphous silicon-based double-junction solar cells.

To study the effect of bandgap variation, we made three double-junction samples in which the bottom cells have a constant bandgap of 1.55 eV (L4781), 1.50 eV (L4786), and 1.41 eV (L4801), respectively, and the top cells were made from 1.75 eV a-Si:H material using the same deposition parameters. These samples were deposited onto stainless steel/textured silver/zinc oxide substrates using the conventional RF glow discharge technique. The thickness of the top cells was made small so that the fill factor is high and the current of the double-junction device is limited by the top cell. This would allow us to evaluate the effect of the bottom cell on the stability of the double-junction structure. The initial performance of these devices measured under a global AM1.5 solar simulator is listed in Table 8. It is noted from the quantum efficiency data that the current is limited by the top cell, and the mismatch between the top and bottom cells ranges from 1.5 to 3 mA/cm².

We have also made a double-junction device (L4808) in which the thickness of the top cell was made larger such that the top cell current is nearly the same as that of the bottom cell. In this case, we have used the 1.55 eV a-SiGe:H cell in the bottom cell. The initial performance of the double-junction device is also listed in Table 8. The quantum efficiency data confirms that the two currents are nearly matched.

These samples were then light-soaked with one-sun illumination at 50 °C under open-circuit condition for 600 hours. Their degraded J-V characteristics and quantum efficiency data are also listed in Table 8.

28

Table 8. Initial and Stabilized Photovoltaic Characteristics of Various Dual-gap, Double-junction Devices.

Sample	State	J_{sc} (mA/cm²)	V_{oc} (V)	FF	η (%)	Q (mA/cm²)
L4801	Initial	9.60	1.60	0.73	11.21	9.35/12.27
(1.41 eV)	600 hrs	9.52	1.55	0.68	9.97	9.21/11.71
L4786	Initial	9.70	1.65	0.74	11.84	9.47/11.42
(1.50 eV)	600 hrs	9.70	1.59	0.67	10.36	9.46/10.86
L4781	Initial	9.67	1.68	0.74	12.02	9.43/10.89
(1.55 eV)	600 hrs	9.66	1.61	0.66	10.24	9.29/10.65
L4808	Initial	10.05	1.66	0.70	11.68	10.24/10.49
(1.55 eV)	600 hrs	9.98	1.60	0.62	9.88	10.07/10.38

Each sample consists of several 0.25 cm² active-area devices. The measurements were made using a single-source AM1.5 solar simulator at 25 °C. The Q-values refer to the top cell and the bottom cell, respectively.

One can readily make the following observations:

1. On the initial performance of L4781, L4786, and L4801:

    a. As the bandgap of the bottom cell decreases, V_{oc} also decreases as expected. Sample L4801, which has the narrowest bandgap in the bottom cell, exhibits the largest current mismatch between the component cells.

    b. J_{sc} and fill factor are similar for the three devices because of the same deposition parameters used for the current-limiting top cells.

    c. The initial efficiency of the double-junction devices is hence essentially dependent on V_{oc}. Sample L4781, which has the least Ge in the bottom cell, shows the highest initial efficiency.

2. The initial performance of sample L4808, which has the same bottom cell as L4781, exhibits a higher J_{sc} value because of the thicker top cell. However, the fill factor of the devices is lower than the other three samples due to the closer match. Its V_{oc} is also slightly smaller than L4781 due to the thicker top cell.

3.   On the degraded J-V characteristics of samples L4781, L4786, and L4801:

   a.   Sample L4801, which has the narrowest bandgap in the bottom cell, shows the lowest V_{oc}, consistent with the initial performance.

   b.   Sample L4801 has a slightly better fill factor due to the larger current mismatch.

   c. J_{sc} remains similar for the three samples.

   d.   The percentage of degradation and stabilized efficiencies are similar for the three samples.

4.   The degraded performance of sample L4808, which has a thicker top cell than L4781, shows a lower fill factor due to closer matched component cells, and J_{sc} remains higher due to the thicker top cell.

From the above analysis, one can see that in order to achieve a higher stabilized efficiency, one should current-limit the top cell. The desired amount of mismatch depends on the performance of the bottom cell. If the performance of the bottom cell is improved, the mismatch can be reduced, and one can then take advantage of a thicker top cell for higher J_{sc} without losing too much on the fill factor.

We have designed a double-junction device in which we have incorporated a profiled bandgap structure in the bottom a-SiGe:H cell which we have previously shown to improve solar cell performance.[32] The bandgap in the narrowest region is 1.41 eV, and the top cell is 1.75 eV a-Si:H. The initial performance of this device is listed in Table 9. After 600 hours of one-sun illumination at 50°C, the stabilized active-area efficiency as measured under global AM1.5 single-source simulator at 25 °C is 11.16%, which we believe is the highest value reported to date on double-junction amorphous silicon alloy solar cells. A similarly degraded cell, measured at NREL under a dual-source simulator, showed an active-area efficiency of 10.4%.

Table 9.   Initial and Stabilized Photovoltaic Characteristics of a Dual-gap, Double-junction 0.25 cm² Device with Profiled Bandgap in the Bottom Cell.

Sample	State	J_{sc} (mA/cm²)	V_{oc} (V)	FF	Active Area (cm²)	η (%)
L4789	Initial	10.67	1.650	0.716	0.2465	12.61
	600 hrs	10.61	1.606	0.655	0.2465	11.16

In summary, we have studied the stability of various double-junction solar cells in terms of the bandgaps of the bottom cells and current mismatch between component cells. We have used a bandgap profiling structure as well as a current mismatch approach and obtained a high stabilized conversion efficiency of 11.16%.

Section 4

Large-Area Deposition Research
and Module Research

Introduction

The 2B machine has been used to prepare cells for large-area (~ 900 cm^2) module fabrication. The major emphasis was toward the development of high-efficiency, dual-bandgap, double-junction cells. Some exploratory work has also been done on triple-bandgap, triple-junction devices. The top cell in both structures consists of an a-Si:H i layer, and the middle and bottom cells have a-SiGe:H alloy i layers. The back reflector is stainless steel/Ag/ZnO.

The cell fabrication procedure consists of first preparing the back reflector using sputter deposition technique. The coated area is greater than 900 cm^2. The n, i, and p layers are then deposited in the 2B machine. The coated substrate is either cut into smaller pieces for (1) small-area cell research or processed as such for (2) large-area (~ 900 cm^2) module research.

Small-area (0.25 cm^2) Cell Research

The large-area coated substrate is cut into 2" x 2" pieces, and ITO dots are deposited onto the substrate using an evaporation mask. Finally, silver grid lines are deposited by evaporation through a mask. The active device area in this case is ~ 0.25 cm^2.

The purpose of the small-area research is to separate the effects of the subsequent module fabrication steps from the basic material quality, thereby making the comparison of the 2B cells with the cells made in the small-area deposition system (LINE) possible. Also, the smaller size of the devices and substrates enables us to evaluate a large number of cells for light-induced degradation.

Status of December 1991

The status of different types of cells and modules at the end of December 1991 and reported in the Phase I Annual Technical Progress Report is summarized in Table 10.

Table 10. Status of Cells/Modules Reported in Phase I Annual Report (December 1991).

Cell Type	Area (cm²)	Run No.	Back Reflector	V_{oc} (V)	J_{sc} (mA/cm²) [from Q]	FF	Efficiency (%)
a-Si:H	0.25	454	Ag/ZnO	0.915	16.57	0.636	9.64
a-SiGe:H	0.25	693	Ag/ZnO	0.732	20.16	0.606	8.94
Double-junction	0.25	703	Ag/ZnO	1.639	9.76 [Q_T=9.83] [Q_B=9.93]	0.690	11.04
Triple-junction	0.25	657	Ag/ZnO	2.334	6.54 [Q_T=6.73] [Q_M=6.58] [Q_B=7.28]	0.656	10.02
Double-junction (stabilized efficiency)	0.25	519	Ag/ZnO	1.54	8.70	0.61	8.10
Double-junction module	921	588	Ag/ZnO	1.64	I_{sc}=8.55 A	0.580	8.20

Briefly, the efficiencies of the small-area a-Si:H single-junction, a-SiGe:H single-junction, a-Si:H/a-SiGe:H double-junction, a-Si:H/a-SiGe:H/a-SiGe:H triple-junction cells and the module were 9.64%, 8.94%, 11.04%, 10.02% and 8.20%, respectively. The stabilized small-area, double-junction efficiency after 520 hours of one-sun 50 °C exposure was 8.10%.

Progress of January 1992 - February 1993

Considerable progress has been made in improving the efficiency of different types of devices made in the 2B machine. The methodology used was to compare the performance of the top cell, the bottom cell and the multijunction cells with the corresponding cells made in the LINE machine. In the past, the LINE machine had consistently outperformed the 2B machine in terms of both material quality and devices. Careful evaluation and analysis of the devices made in the two machines elucidated the shortcomings in the 2B machine. Major changes were made both in the hardware and the deposition parameters of the 2B machine. Some of the analysis of the devices is summarized below.

The efficiency of small-area (~ 0.25 cm²), dual-gap, double-junction cells made in the 2B machine was typically 11.0%-11.4%. In comparison, the corresponding efficiency for the LINE machine is ~ 12.0%-12.5%. A detailed and systematic study was undertaken involving deposition of the various layers n_1, i_1, p_1, n_2, i_2 and p_2 in different combinations in the 2B and LINE machines. The subscripts 1 and 2 refer to the order of deposition, not the order of light penetration. The results are summarized in Table 11. The double-junction device #1384 was fabricated entirely in the 2B machine. The double-junction hybrid sample #1389H was fabricated by depositing the bottom cell (n_1, i_1, p_1) in the 2B machine and the top cell
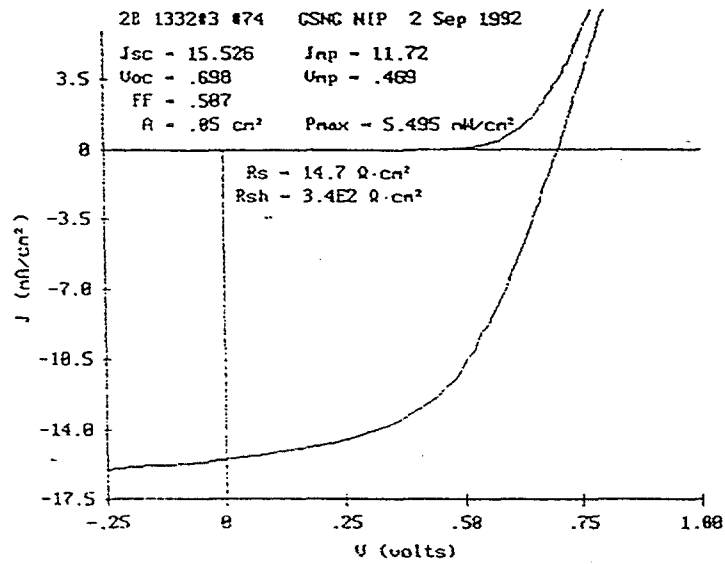
32

(n_2, i_2, p_2) in the LINE machine. The double-junction hybrid device #1395H was prepared by depositing the n_1 and i_1 layers in the 2B machine and the remaining p_1, n_2, i_2, p_2 layers in the LINE machine. The table shows that the hybrid cell 1395H has the highest value of V_{oc} (1.642 V), and the cell 1384 shows the lowest V_{oc} (1.582 V). The results suggest that the tunnel junction (p_1 n_2) is inadequate for the sample 1384 since there is a loss in V_{oc}. After optimization of the component cells made in the 2B machine, it was confirmed that single-junction $n\ i\ p$ cells (both a-Si:H and a-SiGe:H) exhibit similar performance in the two machines. (The comparison is not shown here.) It was, therefore, concluded that the p_1 layer made in the 2B was of poor quality.

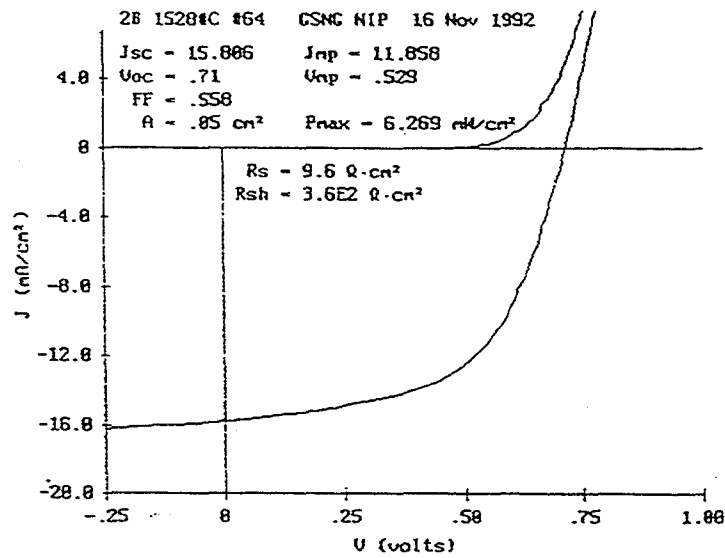**Table 11. Comparison of Small-area 2B-LINE Hybrid Cells.**

Cell Structure	Sample	Efficiency %	J_{sc} (mA/cm^2)	V_{oc} (V)	FF
$n_1\ i_1\ p_1\ n_2\ i_2\ p_2$ made in 2B	1384	10.77	10.08	1.582	0.681
$n_1\ i_1\ p_1$ (2B) + $n_2\ i_2\ p_2$ (LINE)	1389H	10.77	9.79	1.616	0.681
$n_1\ i_1$ (2B) + $p_1\ n_2\ i_2\ p_2$ (LINE)	1395H	11.20	9.80	1.642	0.696

It may be noted that the p_1 layer made in both machines is microcrystalline in nature. The quality of this layer has to be excellent in order to form a good tunnel junction at the p_1 n_2 interface. The tunnel junction is basically a back-to-back reverse-biased junction with respect to the rest of the double-junction device. A poor tunnel junction will have a deleterious effect on the J-V characteristics of the entire device. In order to understand the behavior of the tunnel junction, several structures were investigated. It was found that the I-V characteristics of the $n_1\ i_1\ p_1\ n_2$ structure depended sensitively on the quality of the $p_1\ n_2$ tunnel junction.

The improvement of the p_1 layer was accomplished in two stages. First, the design and the materials used in the p-chamber of the 2B machine were suspect, and, therefore, the entire chamber was upgraded. This included the installation of a new cathode assembly, substrate heater, feedthroughs, etc. Second, the deposition parameters of the p layer were investigated over a wide range of parameters for the purpose of optimization. The J-V characteristics of the $n_1\ i_1\ p_1\ n_2$ structure before and after the changes are shown in Fig. 15. Figure 15(a) shows the J-V characteristics before the changes, and the values of fill factor and series resistance are 0.507 and 14.7 ohms/cm^2, respectively. In contrast, the fill factor and series resistance obtained after the changes are 0.558 and 9.6 ohms/cm^2, respectively (see Fig. 15(b)). The results shown in Fig. 15(b) agree well with corresponding data (not shown here) of the $n_1\ i_1\ p_1\ n_2$ structure made in the LINE machine.

(a)

2B 1332#3 #74   GSNC NIP 2 Sep 1992

Jsc = 15.526   Jmp = 11.72
Voc = .698   Vmp = .469
FF = .587
A = .05 cm²   Pmax = 5.495 mW/cm²

Rs = 14.7 Ω·cm²
Rsh = 3.4E2 Ω·cm²

J (mA/cm²)

V (volts)

(b)

2B 1528#C #64   GSNC NIP 16 Nov 1992

Jsc = 15.886   Jmp = 11.858
Voc = .71   Vmp = .529
FF = .558
A = .05 cm²   Pmax = 6.269 mW/cm²

Rs = 9.6 Ω·cm²
Rsh = 3.6E2 Ω·cm²

J (mA/cm²)

V (volts)

Figure 15.   J-V characteristics of n_1, i, p, n_2 structure of a 0.05 cm² device made in the 2B machine (a) before changes and (b) after changes.

It may be noted that corresponding hardware changes were made in the i- and n-chambers as well as in the 2B machine. The following summarizes the performance of both single-junction and double-junction cells made after the hardware and parametric changes in the 2B machine.

The J-V characteristics and Q curve of a thin single-junction a-Si:H cell made on a stainless steel substrate (no back reflector) are shown in Fig. 16. The values of V_{oc}, J_{sc} and FF are 0.960 V, 10.74 mA/cm^2 and 0.737, respectively. The value of J_{sc} is obtained from Q measurements. The corrected value of efficiency η is equal to 7.60%. This cell, deposited on the stainless steel substrate, simulates the top cell of a dual-bandgap, double-junction cell as regards the amount of reflected light from the substrate. The thickness of the cell has been adjusted to yield a value of $J_{sc} \sim 10.5$ mA/cm^2 which is approximately the value of J_{sc} expected from the double-junction cell.

The J-V characteristics and Q curve of a thicker single-junction a-Si:H cell deposited on a Ag/ZnO back reflector are shown in Fig. 17. The values of V_{oc}, J_{sc} (from Q measurements), FF and corrected η are 0.949 V, 15.77 mA/cm^2, 0.696 and 10.42%, respectively. Note that this thicker cell only qualitatively shows the material quality of the a-Si:H i layer. The deposition parameters have not been optimized to yield the best efficiency.

The J-V characteristics and Q curve of the single-junction bottom a-SiGe:H cell deposited on a Ag/ZnO back reflector are shown in Fig. 18. The values of V_{oc}, J_{sc}, FF and corrected η are 0.739 V, 21.11 mA/cm^2, 0.629 and 9.82%, respectively. The thickness of the i layer has been adjusted such that it could be directly used as the bottom cell of a dual-bandgap, double-junction cell. Thus, Figs. 16 and 18 represent the J-V characteristics and Q curves of the component top and bottom cells, respectively, of a double-junction device.

The J-V characteristics and Q curve of a dual-bandgap, double-junction cell are shown in Fig. 19. The values of V_{oc}, J_{sc}, FF and corrected η are 1.658 V, 10.31 mA/cm^2, 0.707 and 12.08%, respectively. The contribution from the top and bottom cells to the value of J_{sc} are 10.0 and 11.85 mA/cm^2, respectively.

As mentioned earlier, very little work has been done on triple-junction cells during Phase II. All the work was done before the substantial improvements were made in the 2B machine. The J-V characteristics and Q curve of a triple-bandgap, triple-junction cell are shown in Fig. 20. The values of V_{oc}, J_{sc}, FF and η are 2.317 V, 6.90 mA/cm^2, 0.697 and 11.15%, respectively. The contribution to the values of J_{sc} from the top, middle and bottom cells are 6.51, 7.06 and 7.92 mA/cm^2, respectively. Obviously, the performance is relatively poor since none of the improvements have been incorporated so far.
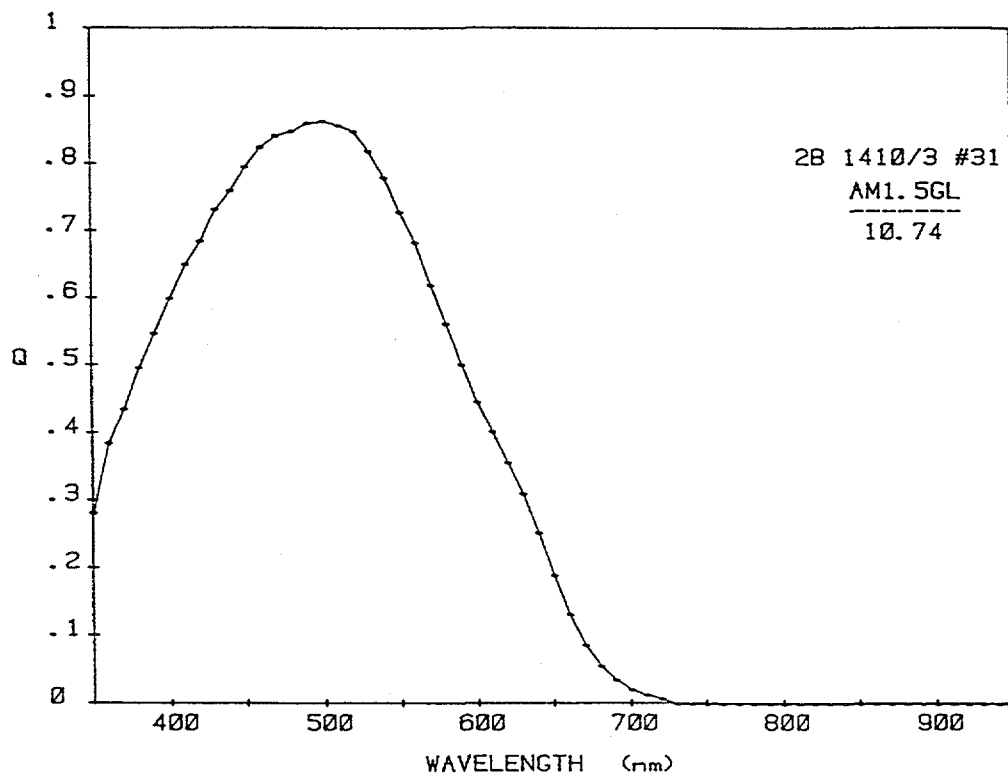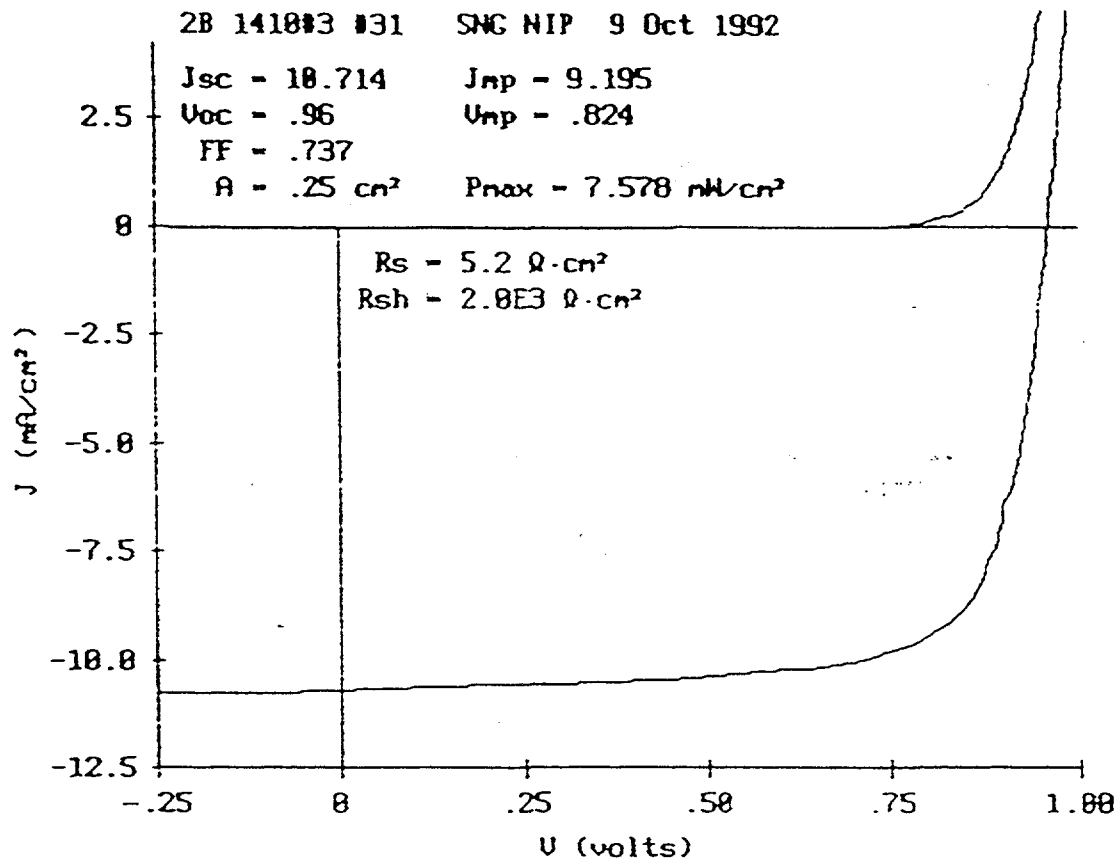
Figure 16. J-V characteristics and *Q* curve of a thin a-Si:H single-junction cell deposited on stainless steel substrate.
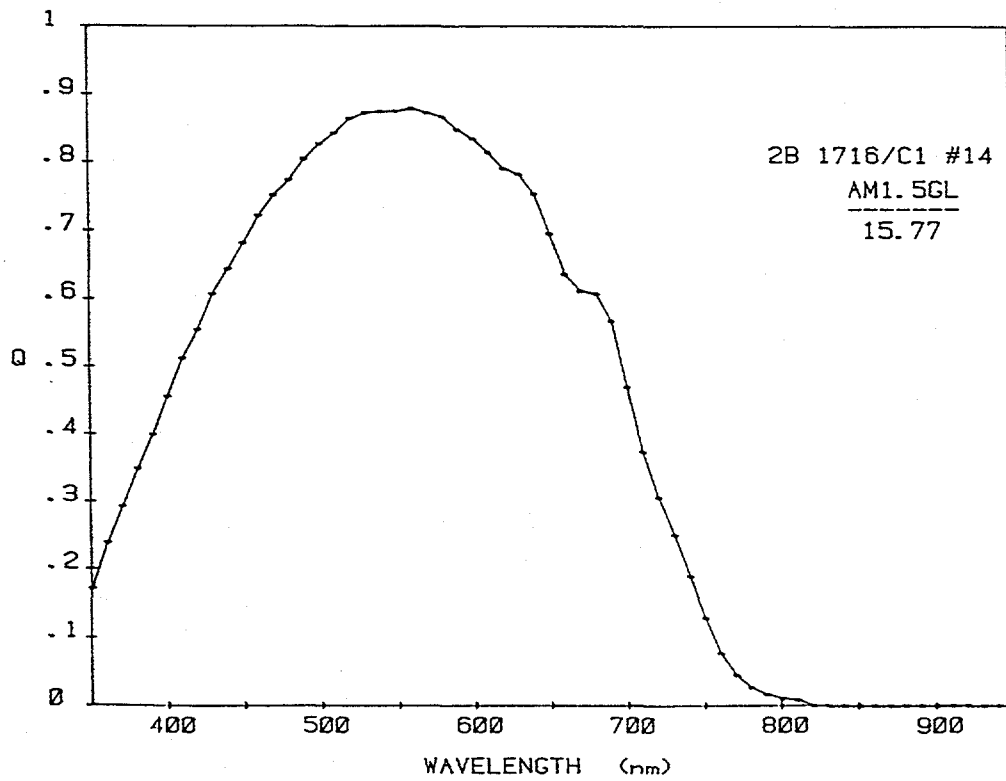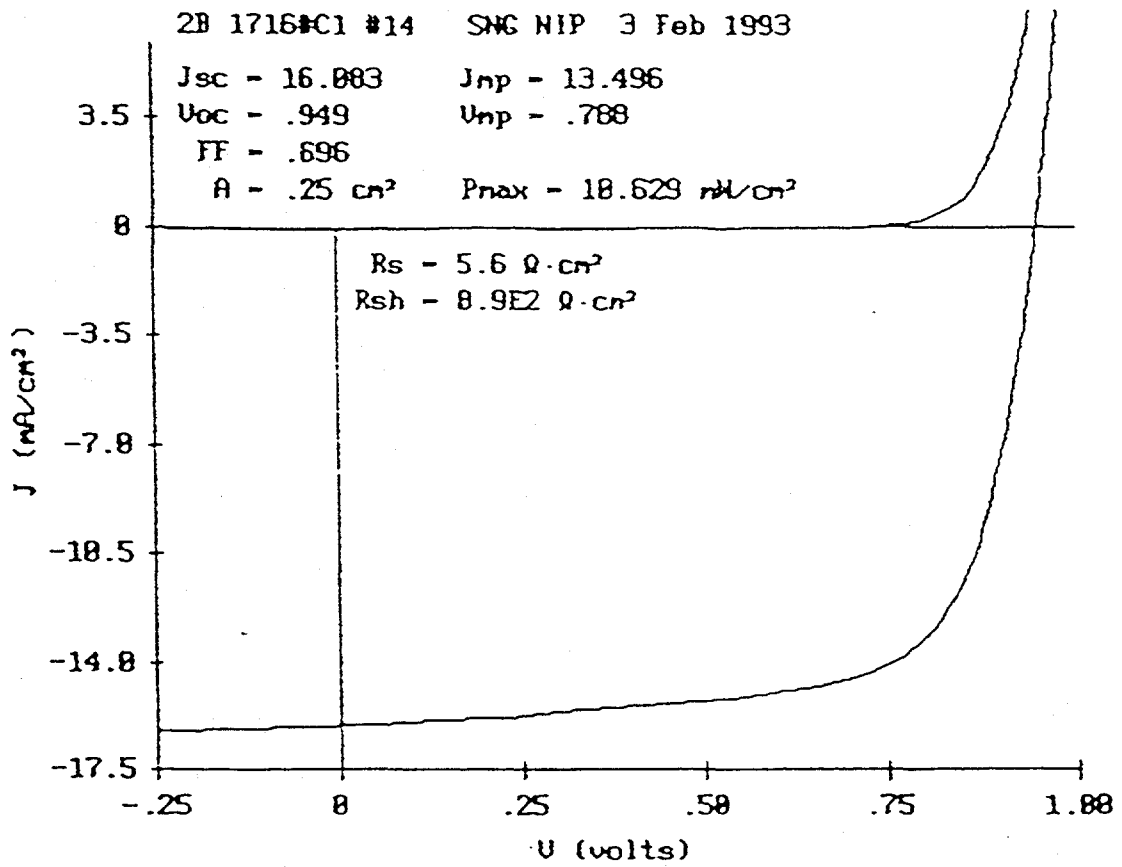
Figure 17. J-V characteristics and Q curve of a relatively thick a-Si:H
single-junction cell deposited on Ag/ZnO back reflector.

2B 1706#01 #14   GSWG NIP   1 Feb 1993

Jsc - 28.964   Jmp - 17.119
Voc - .739   Vmp - .569
 FF - .629
  A - .25 cm²   Pmax - 9.74 mW/cm²

Rs - 5.8 Ω·cm²
Rsh - 6.8E2 Ω·cm²

J (mA/cm²)

4.5
0
-4.5
-9.0
-13.5
-18.0
-22.5

-.25   0   .25   .50   .75   1.00

U (volts)

2B 1706/01 #14
AM1.5GL
————
21.11

Q.

1
.9
.8
.7
.6
.5
.4
.3
.2
.1
0

400   500   600   700   800   900

WAVELENGTH   (nm)

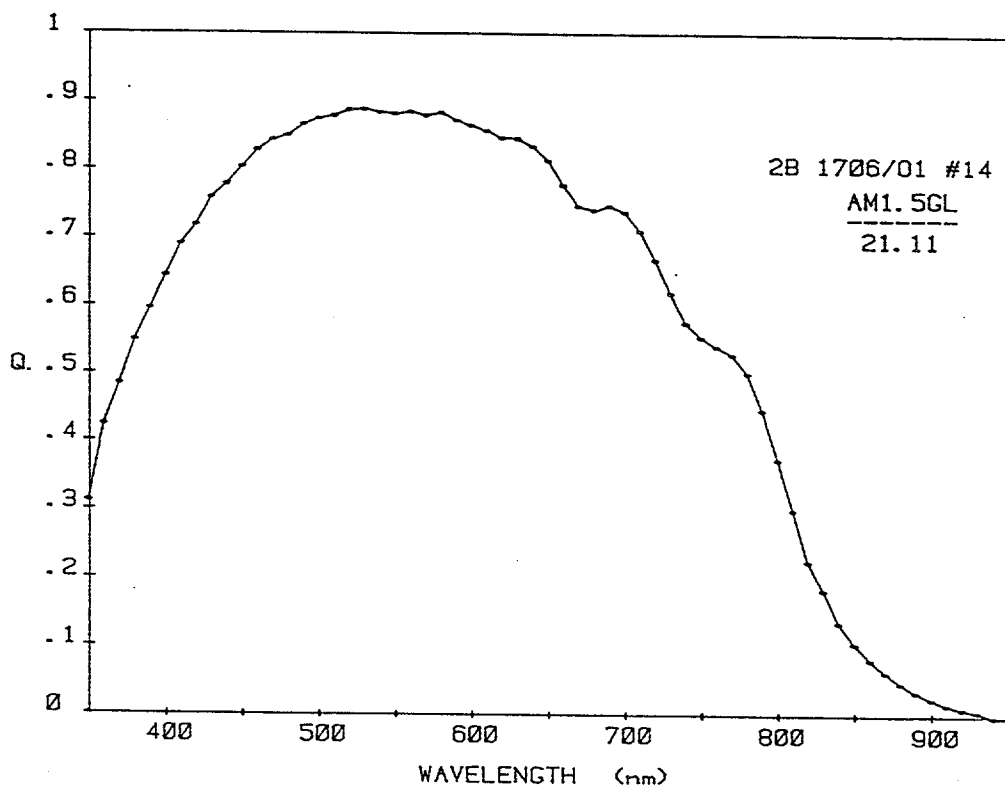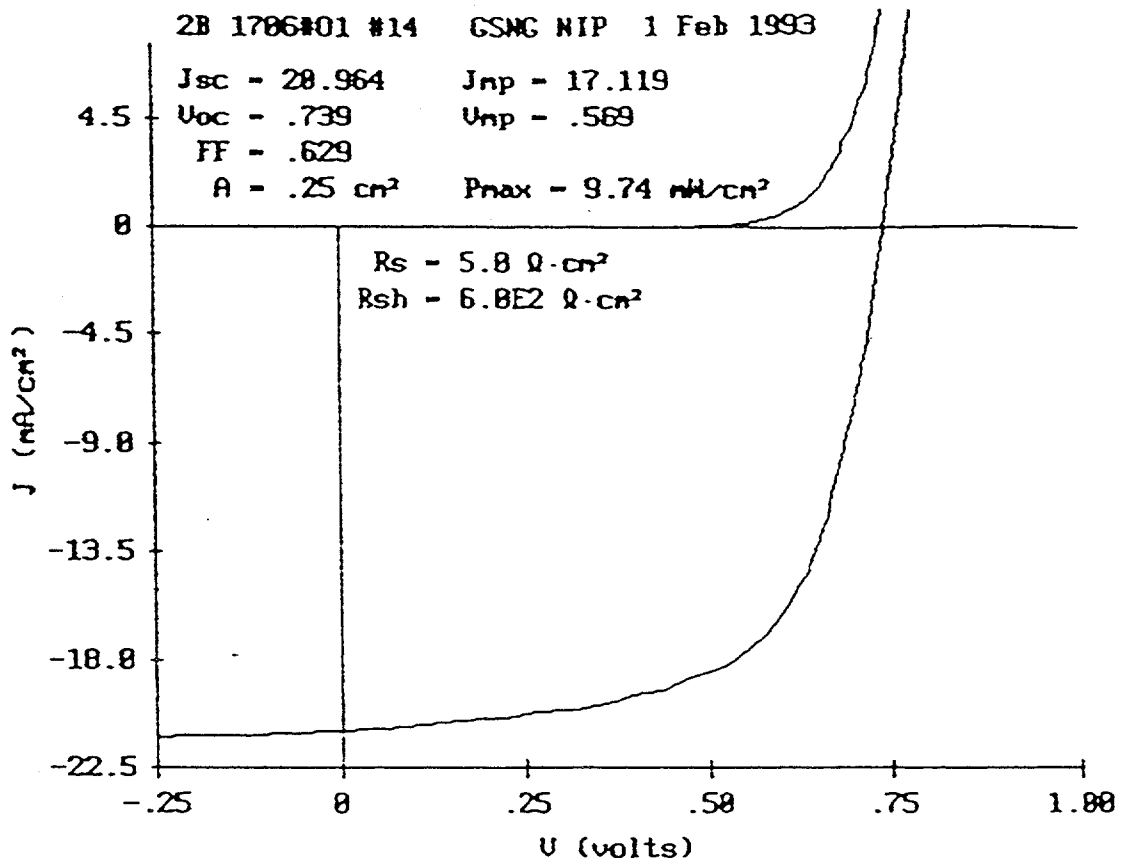**Figure 18.   J-V characteristics and *Q* curve of an a-SiGe:H single-junction cell on a Ag/ZnO back reflector.**
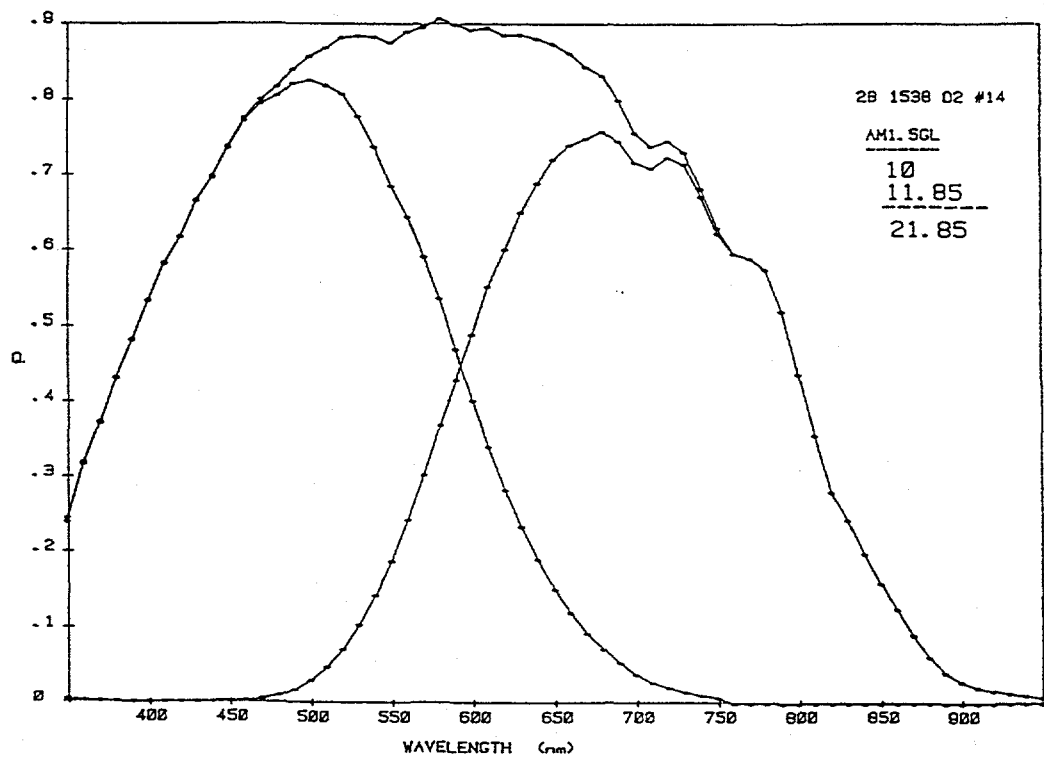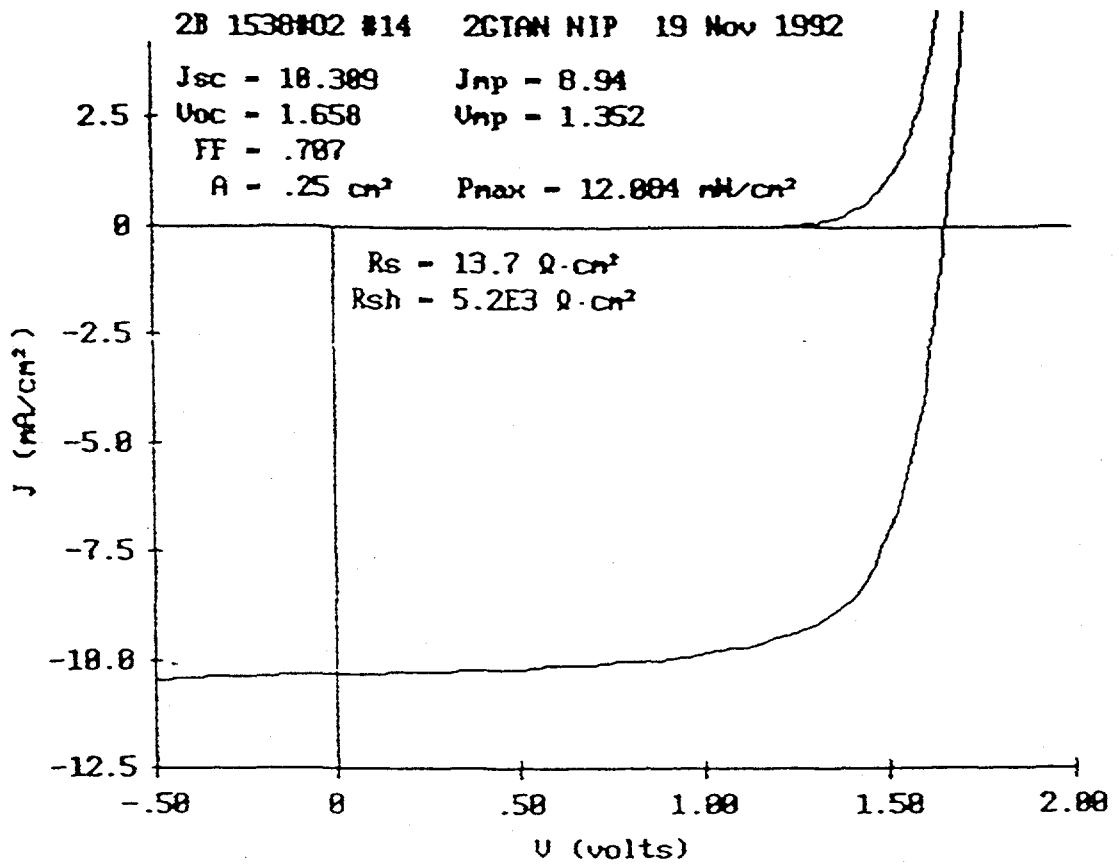
38

Figure 19. J-V characteristics and *Q* curve of a dual-bandgap, double-junction cell on a Ag/ZnO back reflector.
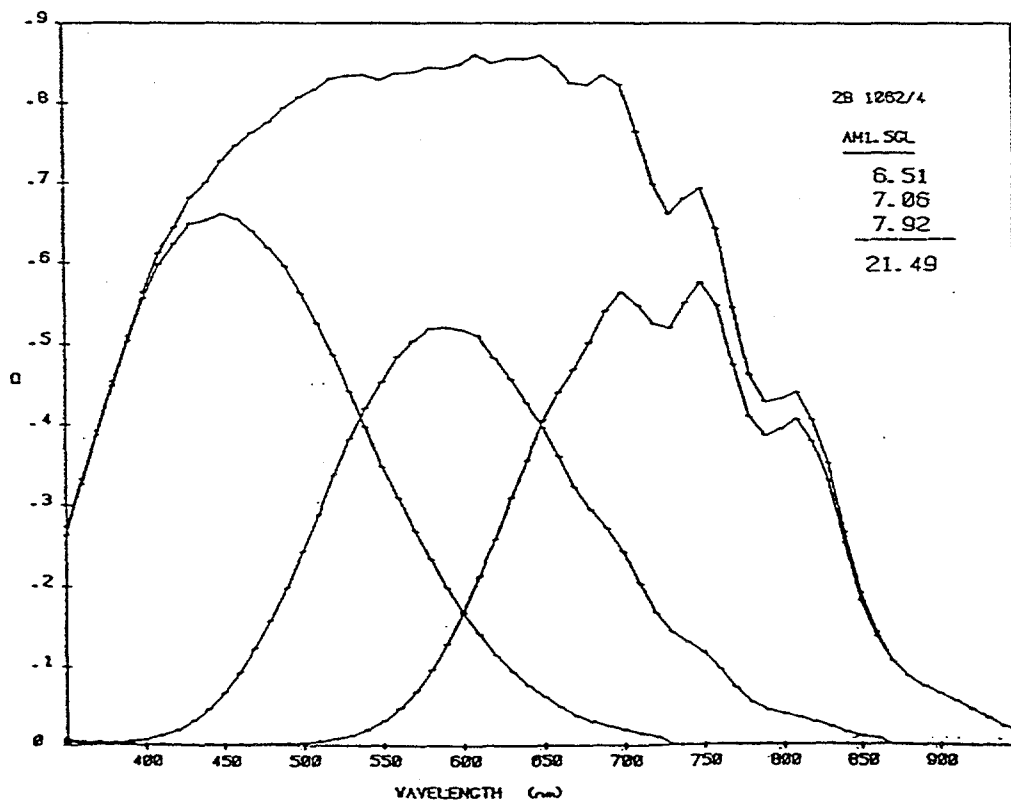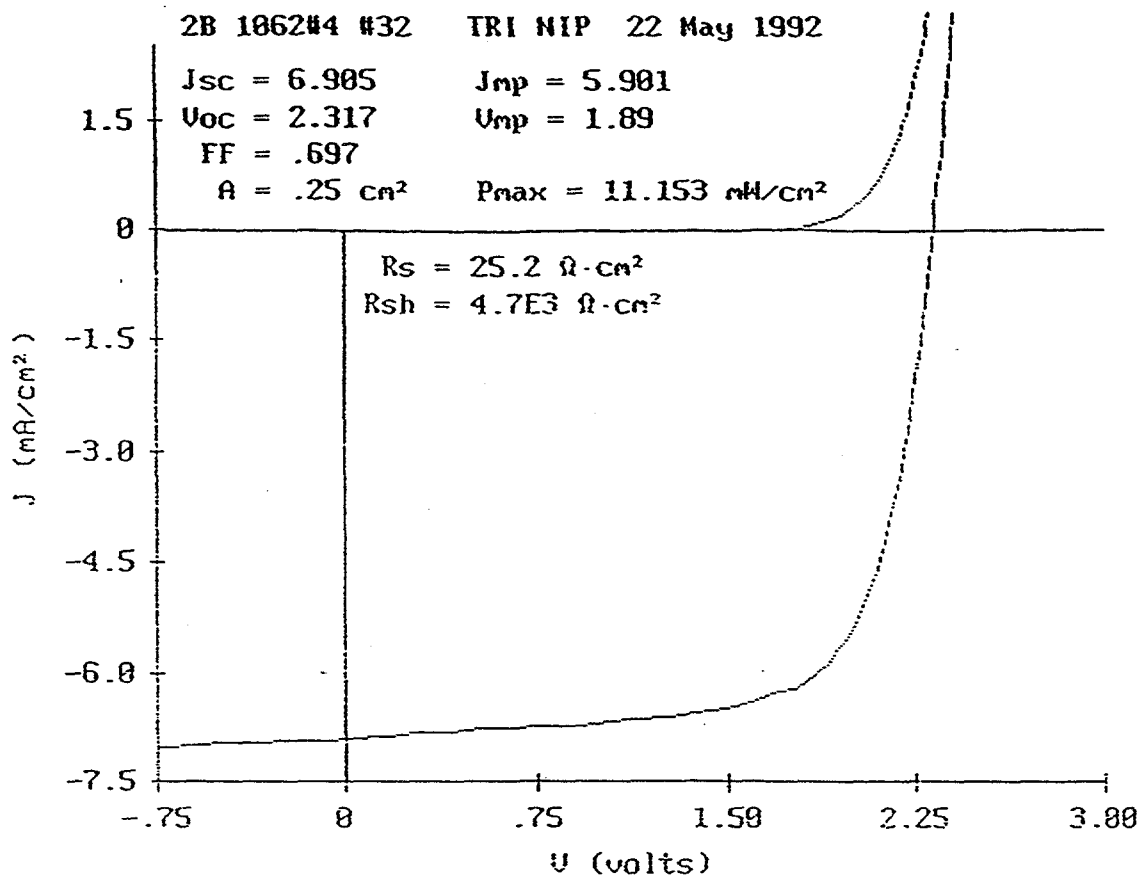
Figure 20. J-V characteristics and *Q* curve of a triple-bandgap, triple-junction cell on a Ag/ZnO back reflector.

Stability of Small-area Cells

The improved dual-bandgap, double-junction, small-area cells have been subjected to one-sun 50 °C light-induced degradation. The results are summarized in Table 12.

Table 12. Stability Results of Dual-bandgap, Double-junction Cells.

Time	Sample No.	Exposure (hours)	Initial Efficiency (%)	Stabilized Efficiency (%)	Degradation (%)
February 1993	1538	764	12.0	10.3	14
June 1992	1031	636	11.1	9.1	18
December 1991	519	520	9.7	8.1	17

The status toward the end of Phase II (February 1993) is that the high efficiency cells degrade from ~ 12.0% to ~ 10.3%, which corresponds to a degradation of ~ 14%. The stabilized efficiency of 10.3% on the small-area cells implies a stabilized 1-sq.-ft. module efficiency of 9.0%-9.5%. The derating factor used for this calculation takes into account the additional losses which are applicable only for the modules. For the purpose of comparison, the status of stability of corresponding cells at the end of June 1992 and the end of December 1991 are also summarized in Table 12. The results establish that the stabilized efficiency has continuously increased from 8.10% to 10.3% in one year.

Large-area (~ 900 cm^2) Module Research

Several batches of dual-bandgap, double-junction modules of aperture area ~ 900 cm^2 have been fabricated. Each improvement made in the small-area cell efficiency has been associated with the fabrication of a batch of modules. The last batch was made after the attainment of 12.0% double-junction, small-area cell efficiency. The results are summarized in Table 13.

41

Table 13. Summary of Initial, Non-stabilized Module Results.

| Module	Aperture Area (cm^2)	Eff (%) USSC Spire	V_{oc} (V)	I_{sc} (A)	FF
1529	904.1	10.0	1.62	8.62	0.649
1533	902.3	9.9	1.64	8.39	0.648
1534	904.4	9.7	1.63	8.31	0.652
1539	904.4	9.9	1.66	8.30	0.653
1540	901.7	10.2	1.65	8.52	0.651
1543	899.7	9.8	1.62	8.55	0.640
1544	902.4	10.4	1.66	8.33	0.680
1548	902.0	10.0	1.67	8.49	0.636
1549	902.6	10.6	1.67	8.66	0.661
1550	902.1	10.3	1.66	8.51	0.660

The I-V measurements were made in the USSC Spire Solar Simulator Model 240A equipped with a peak detector circuit board. Module #1549 with aperture area 902.6 cm^2 exhibits the highest efficiency of 10.6%. The I-V characteristics of this module are shown in Fig. 21. The values of V_{oc}, I_{sc} and FF are 1.67 V, 8.66 A and 0.661, respectively. Several modules with efficiency $\geq$ 10.0% have been fabricated as shown in Table 13. It is interesting to note that the yield has been excellent for all modules fabricated. The progress made in the module efficiency since the inception of the USSC NREL program is graphically shown in Fig. 22. Efficiency scatter of the batch of modules made at each period is indicated. It is clear from the graph that the initial module efficiency has increased steadily at a relatively rapid rate.

Status of February 1993

The status of efficiency of small-area cells and large-area modules at the end of February 1993 are summarized in Table 14. The numbers have been taken off Figs. 16-21 and Tables 12 and 13. In order to quantitatively measure the progress made from the end of Phase I to the end of Phase II, the efficiency numbers from Tables 10 and 14 are tabulated in Table 15. Briefly, the efficiency enhancements for the a-Si:H and a-SiGe:H cells are from 9.64% to 10.42% and from 8.94% to 9.82%, respectively. For the double-junction and triple-junction cells, the initial efficiency has gone up from 11.04% to 12.08% and from 10.02% to 11.15%, respectively. The light-induced, one-sun 50 °C stabilized efficiency has increased from 8.10% to 10.30% for double-junction cells. The initial double-junction module efficiency with ~ 900 cm^2 area has gone up from 8.2% to 10.6%. It is clear from the above data that significant progress has been made all across the board.
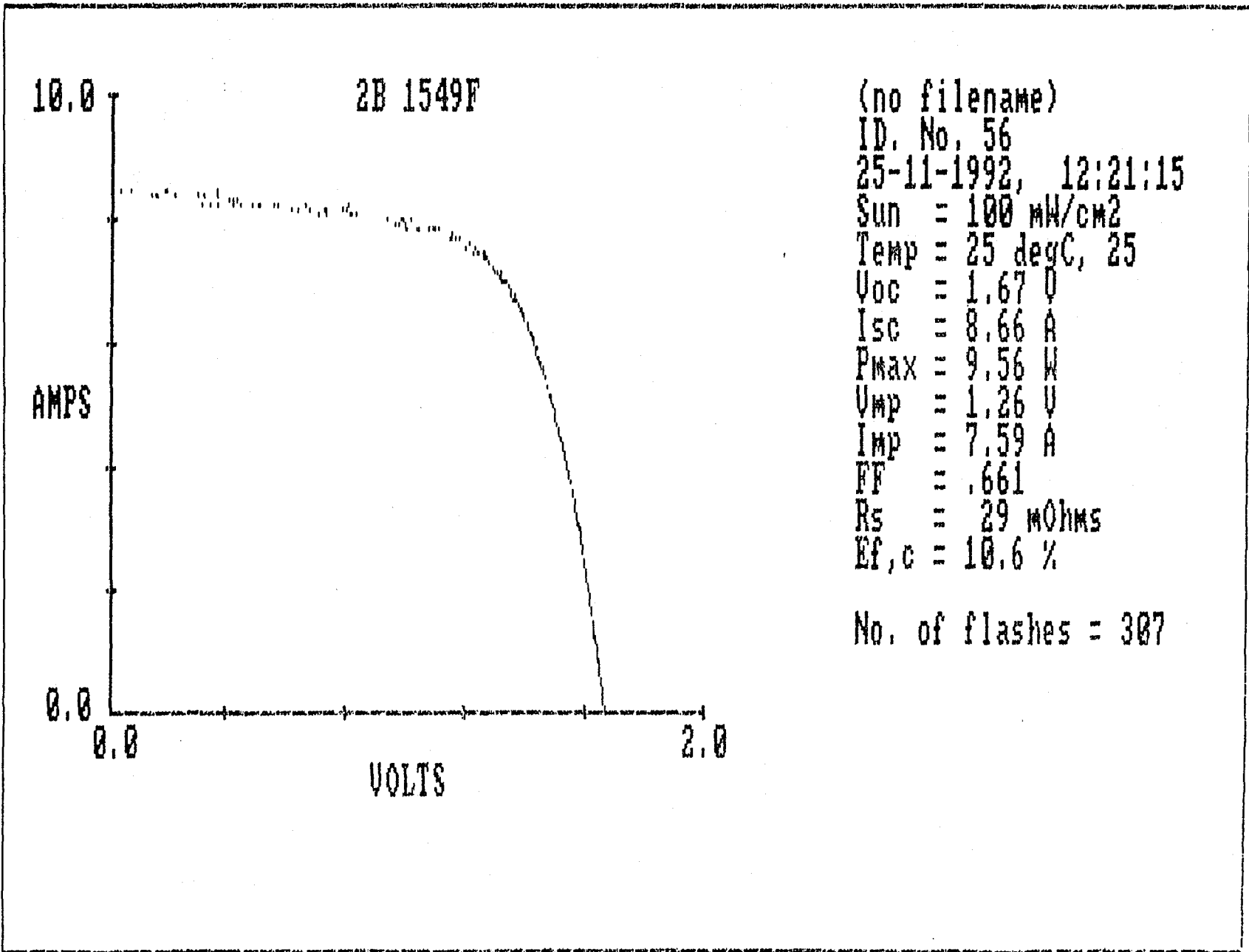
Figure 21. I-V characteristics of 902.6 cm² aperture area module exhibiting 10.6% efficiency.

Progress in Module Efficiency
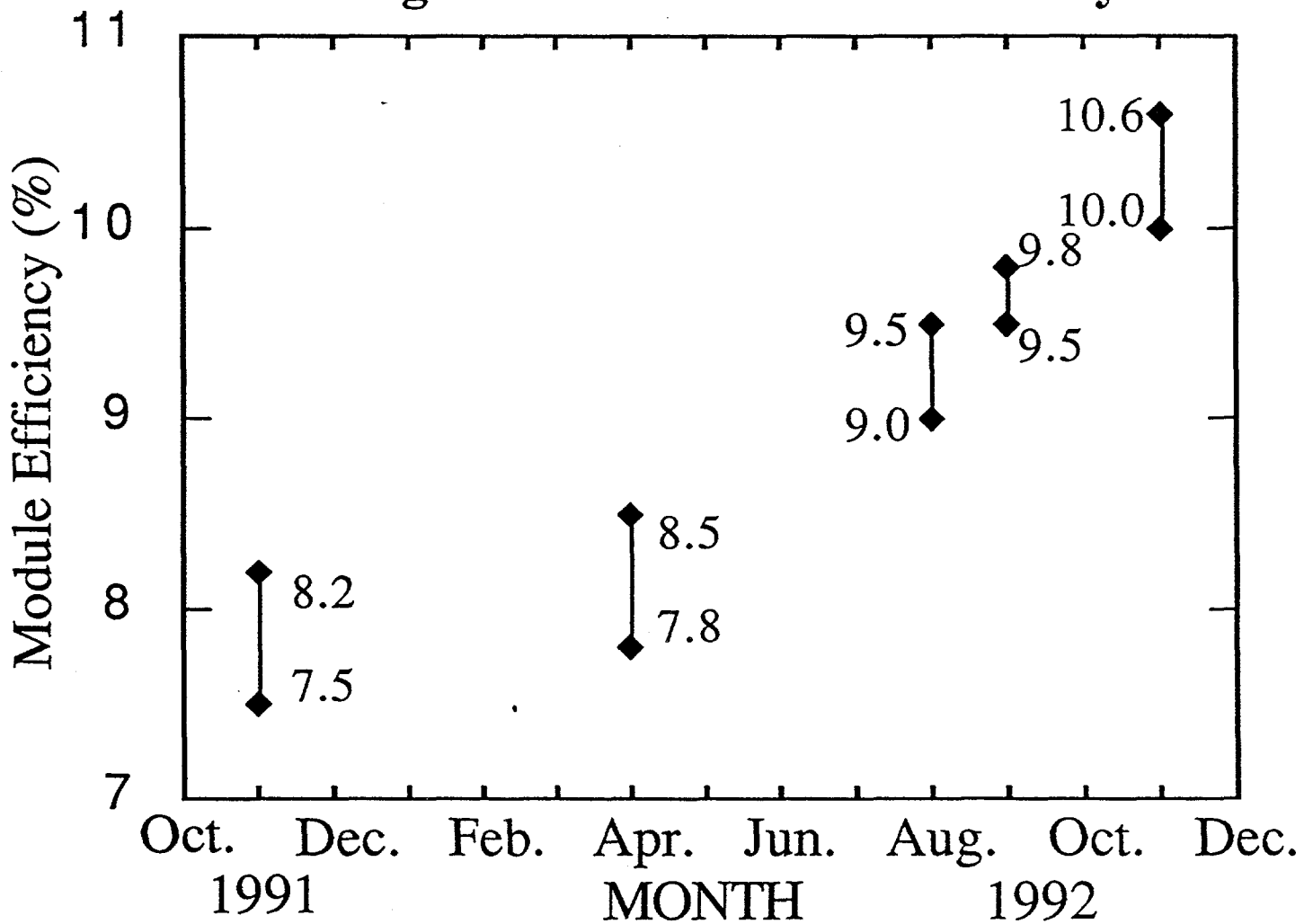
Figure 22. Progress made in module efficiency as a function of time.

Table 14. Status of Cells/Modules at the End of Phase II (February 1993).

Cell Type	Area (cm²)	Run No.	Back Reflector	V_{oc} (V)	J_{sc} (mA/cm²) [from Q]	FF	Efficiency (%)
a-Si:H	0.25	1410	S.S.	0.960	10.74	0.737	7.60
a-Si:H	0.25	1716	Ag/ZnO	0.949	15.77	0.696	10.42
a-SiGe:H	0.25	1706	Ag/ZnO	0.739	21.11	0.629	9.82
Double-junction	0.25	1538	Ag/ZnO	1.658	10.31 [Q_T=10.00] [Q_B=11.85]	0.707	12.08
Triple-junction *	0.25	1062	Ag/ZnO	2.317	6.90 [Q_T=6.51] [Q_M=7.06] [Q_B=7.92]	0.697	11.15
Double-junction (stabilized efficiency)	0.25	1538	Ag/ZnO	1.60	10.30	0.63	10.30
Dbl.-junc. module	902.6	1549	Ag/ZnO	1.67	I_{sc}=8.66 A	0.661	10.60

*Not optimized

Table 15. Summary of Progress Made from the End of Phase I to the End of Phase II.

Cell Type	Area (cm²)	Back Reflector	Phase I Samp. No.	Phase I Eff. (%)	Phase II Samp. No.	Phase II Eff. (%)
a-Si:H	0.25	S.S.			1410	7.60
a-Si:H	0.25	Ag/ZnO	454	9.64	1716	10.42
s-SiGe:H	0.25	Ag/ZnO	693	8.94	1706	9.82
Double-junction	0.25	Ag/ZnO	703	11.04	1538	12.08
Triple-junction *	0.25	Ag/ZnO	657	10.02	1062	11.15
Double-junction (stabilized efficiency)	0.25	Ag/ZnO	519	8.10	1538	10.30
Dbl.-junc. module	900.0	Ag/ZnO	588	8.20	1549	10.60

* Not optimized

Measurements at NREL

Three of the modules listed in Table 13 were sent to NREL for efficiency measurements. These results are summarized in Table 16. The measurements performed at USSC were done with a Spire 240A solar simulator with a peak detector circuit. This circuit was designed by the Spire Corporation for accurate measurement of high-capacitance amorphous silicon modules. The USSC panels were designed to achieve a maximum efficiency, which resulted in an all-parallel configuration. In this parallel configuration, the module would also have the maximum possible capacitance for this type of material.

It may be seen from Table 16 that the NREL outdoor measurements show efficiency values 10% to 12% lower than those measured indoors. We should mention that NREL outdoor measurements are performed under prevailing outdoor conditions and may therefore vary from the standard reporting conditions of AM1.5 and 25° C. With proper spectral corrections, NREL estimates the uncertainty in their outdoor measurements to be within ± 3%. More round-robin tests between outdoor and indoor measurements are necessary to resolve this problem.

Outdoor Measurements

We have done an initial analysis of the possible sources of error associated with the outdoor efficiency measurements as they relate to dual-gap, double-junction a-Si modules. A list of these sources of error with corresponding magnitudes and a brief description follows. The spectral errors are based on modeling and are approximate in magnitude. A positive value in the error bar indicates the module would measure higher efficiency outdoors than under the standard reporting conditions (AM 1.5 global, 25 °C), and for a negative value, the module would measure lower than standard reporting conditions (SRC). It should be pointed out that many of the errors may be minimized by taking proper quality control measures. These include suitable choice of reference cells, measurement of spectral irradiance and use of spectral mismatch as a quality assurance factor (e.g., mismatch factor within 3% for the component cells) and accurate measurement of module temperature.

<u>Measurement and Calibration Effects</u>

A.   Pyronometer irradiance measurement: +3%, -3%

This number is generally quoted as being the best one can typically achieve under carefully controlled conditions.

B.   Module temperature: +0, -1.5%

This is due to the difference between actual module temperatures (derived from open-circuit voltage measurements) and the SRC temperature. The negative value is a result of the module having a maximum response at approximately 25 °C.

In addition, there could be errors associated with the data acquisition system. These include measurement resolution, sweep rate, circuit calibration, etc.

Spectral Effects

In this section we have modeled what effect the full range of reasonable atmospheric parameter variations would have on the error in evaluating the outdoor efficiency of these types of modules. We first calculated the efficiency of the module under the standard AM1.5 global spectrum and then varied the most important atmospheric parameters to evaluate the effect they had on the module efficiency. All of the atmospheric parameters were varied within a range of values that are commonly observed outdoors under clear-sky conditions.

A.   Air Mass: +0%, -2.5%

These modules are designed for the SRC air mass, and the deviations in air mass (pressure corrected) under actual outdoor conditions (within two hours of solar noon) constitute a negative error. The range of air mass values used was 1.0 to 2.7.

B.   Ground albedo: +2.5%, -0%

This parameter could have a maximum effect under winter conditions. The range used was 20% to 80% spectrally invarient.

C.   Aerosol optical depth: +1.5%, -0.5%

The range was 0.05 to 0.4.

D.   Precipitable water vapor:

This parameter depends most significantly on the type of device used to evaluate the total input irradiance. This is because the water vapor content does not significantly affect the amorphous module but could affect the reference device considerably. The range of precipitable water vapor used was 0.4 to 4.0 cm. We have listed the possible variation for three types of devices that could be used to determine the total irradiance.

1. Pyronometer: +6%, -5%

2. x-Si (unfiltered): +3.5%, -3.5%

3. x-Si (filtered): +0%, -1%

It is quite apparent, even from this approximation, that the errors in evaluating these modules outdoors could exceed the 10% level, if adequate precautions are not taken.

Table 16.   A summary of measurements at USSC and NREL. All outdoor measurements (I_{sc}, P_{max} and Eff) have been corrected for pyronometer irradiance measurement only.

Samp. No.	Measurement Conditions	V_{oc} (V)	I_{sc} (A)	FF (%)	P_{max} (W)	Eff (%)
1544	USSC Spire	1.66	8.33	68.0	9.41	10.4
	Outdoor #1	1.64	7.81	65.9	8.46	9.4
	Outdoor #2	1.55	8.05	65.1	8.11	9.0
1549	USSC Spire -	1.67	8.66	66.1	9.56	10.6
	Outdoor #1	1.66	7.93	65.4	8.62	9.6
	Outdoor #2	1.65	8.12	65.0	8.69	9.6
1550	USSC Spire	1.66	8.51	66.0	9.31	10.3
	Outdoor #1	1.64	7.87	63.3	8.15	9.1
	Outdoor #2	1.61	8.11	62.8	8.19	9.1

Large-Area Uniformity Studies

Uniformity studies have been initiated on the 2B machine in order to identify possible efficiency improvements. Figures 23-28 are examples of contour plots which have aided this investigation. Figures 23-26 represent the efficiency, J_{sc}, V_{oc}, and fill factor, respectively. It should be noted that these figures represent only the uniformity of the various parameters. The absolute values of J_{sc} and efficiency are not corrected for either device area or Q measurement. Figure 27 plots the J_{sc} of the top cell deposited on a stainless steel substrate (i.e., no BR). Figure 28 shows the J_{sc} of the bottom solar cell using a cut-on filter to approximately simulate the light seen when this cell is part of a tandem structure. These contour plots illustrate uniformity variation in IV characteristics. They were made by measuring 1 cm^2 areas spread over a 1 ft^2 deposition run and fitting the individual cell data to a grid. The deposition parameters used to make the attached plots were the same as for USSC's highest efficiency module (10.6%). Analysis shows that the center 450 cm^2 region of the tandem efficiency plot (Fig. 23) has 5% greater efficiency than the average over the whole module dimensions. This has been confirmed with mask measurements on actual modules. Two major elements of the non-uniformities are (1) variation characterized by a circular pattern as particularly seen in Figs. 24, 27 and 28 and (2) V_{oc} and FF decrease near gas flow exhaust, as in Figs. 25 and 26. The circular variation has been shown to be primarily due to film thickness variation. We believe that gas flow patterns and cathode geometry contribute to this effect. The V_{oc} and FF decreases are due to a poor tunnel junction in this deposition area. Adjustments to the p-layer deposition parameters will be attempted to mitigate this problem.
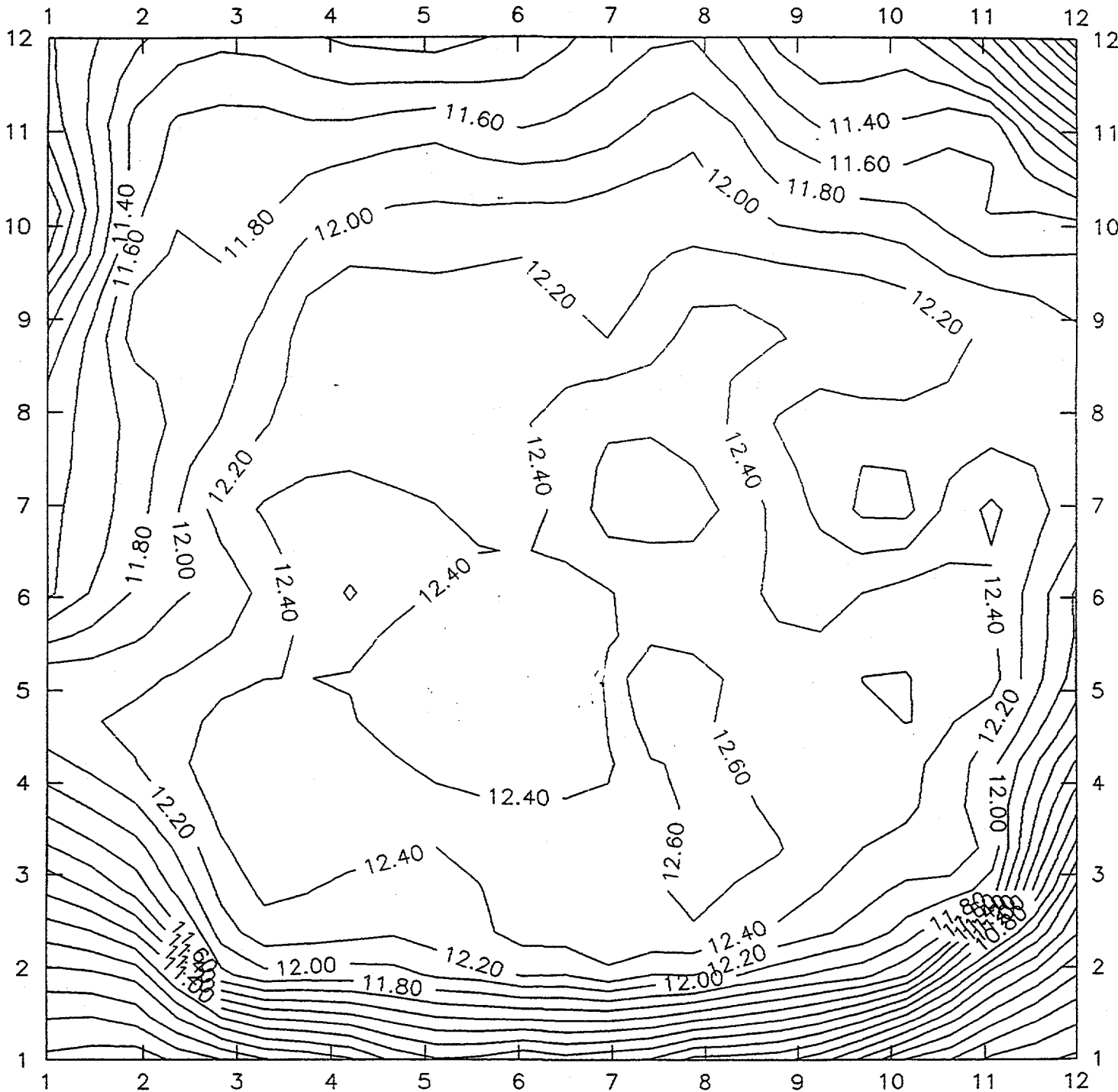
Figure 23.   Efficiency contour plot of 1 sq. ft. double-junction cell.
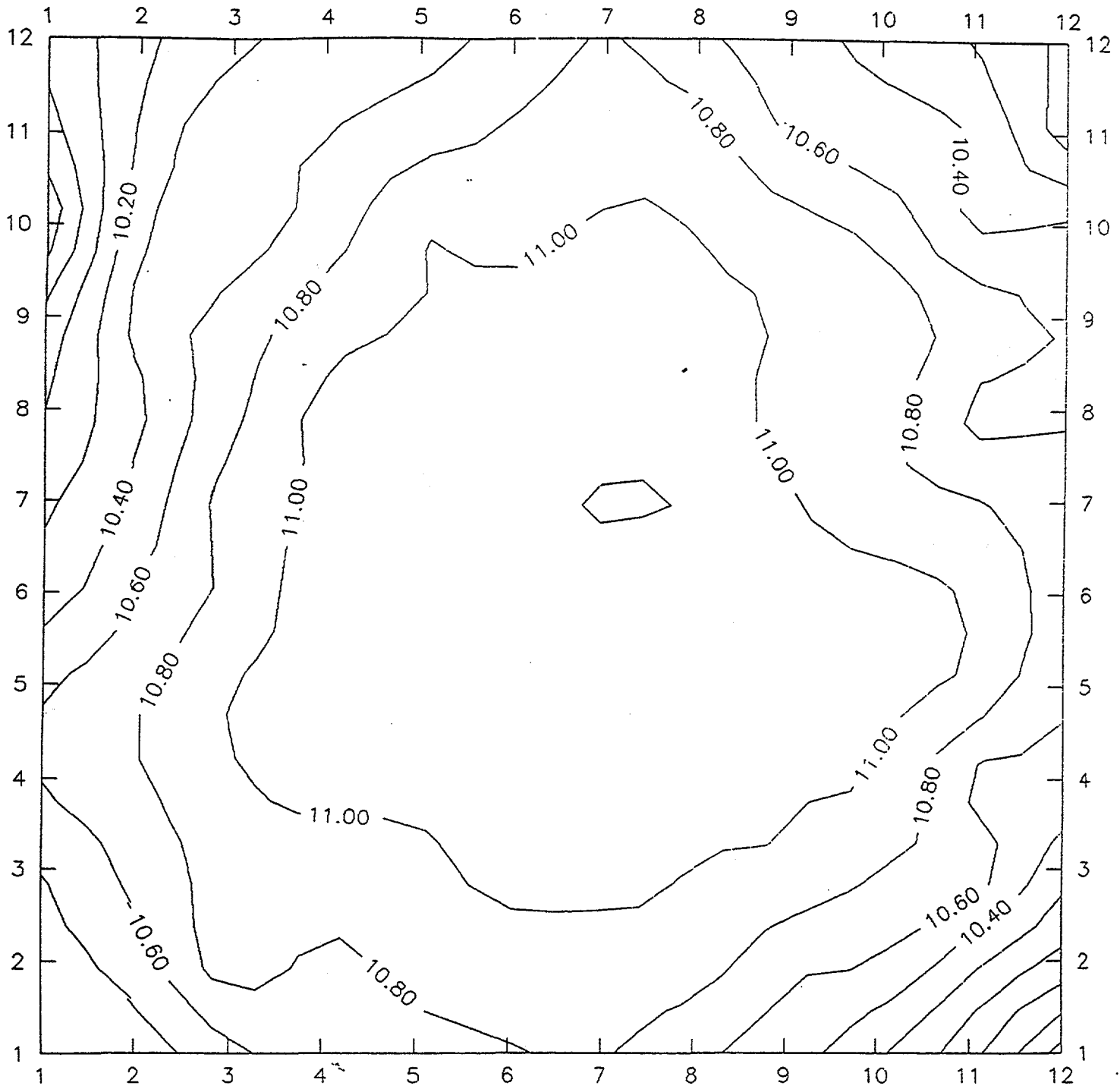
49

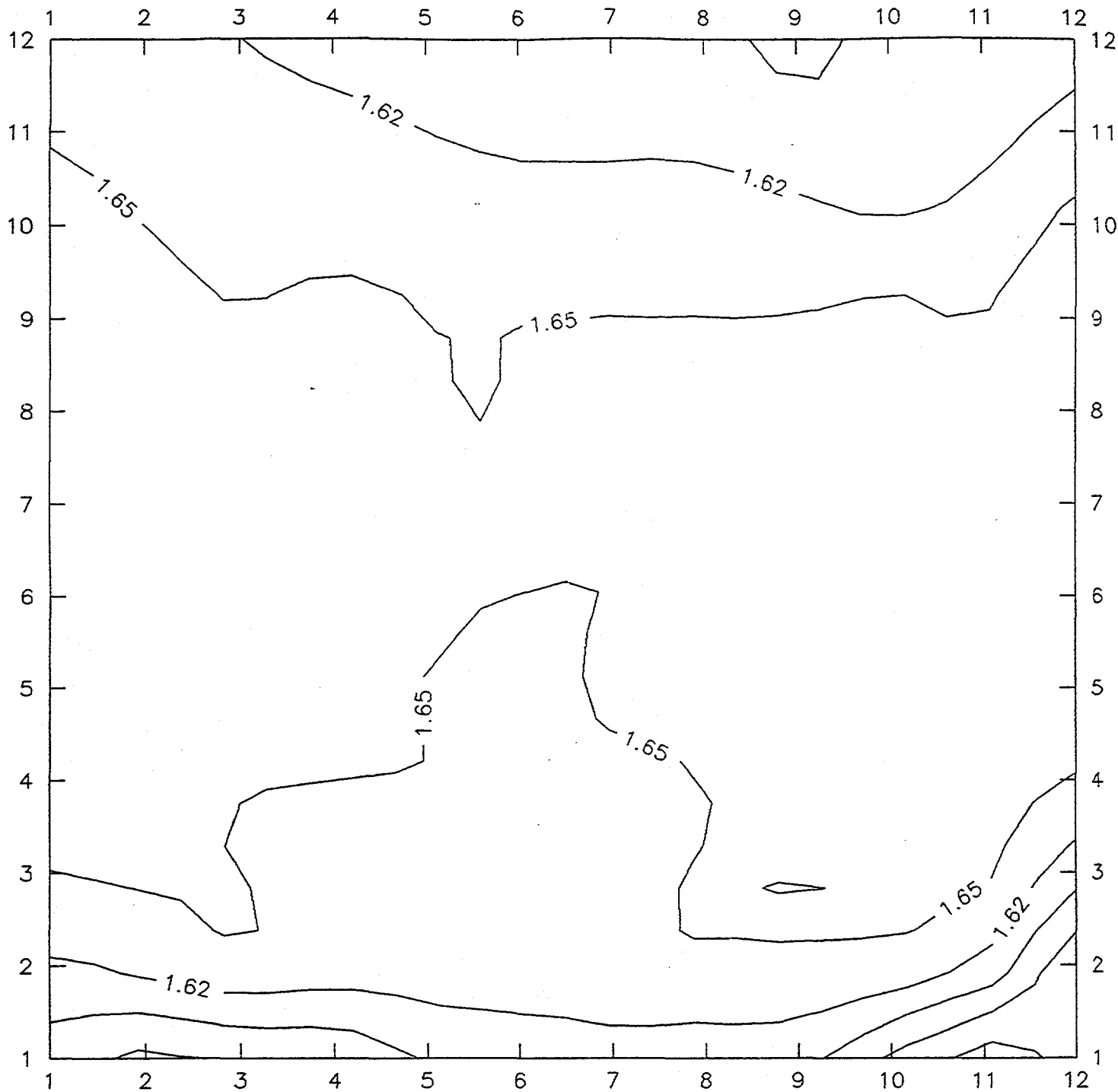**Figure 24. J_{sc} contour plot of 1 sq. ft. double-junction cell.**

50

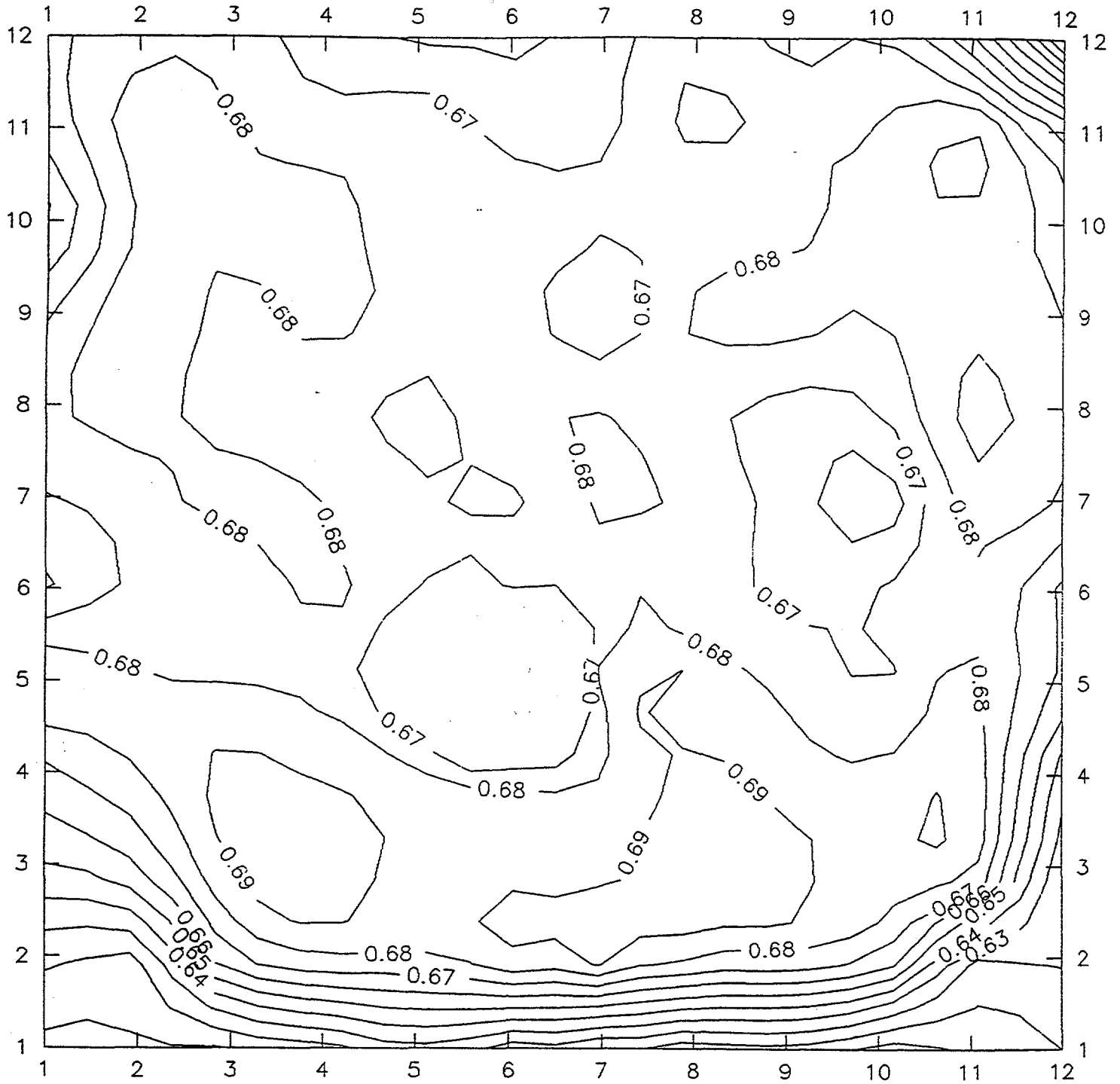**Figure 25.** V_{oc} contour plot of 1 sq. ft. double-junction cell.

Figure 26.   FF contour plot of 1 sq. ft. double-junction cell.
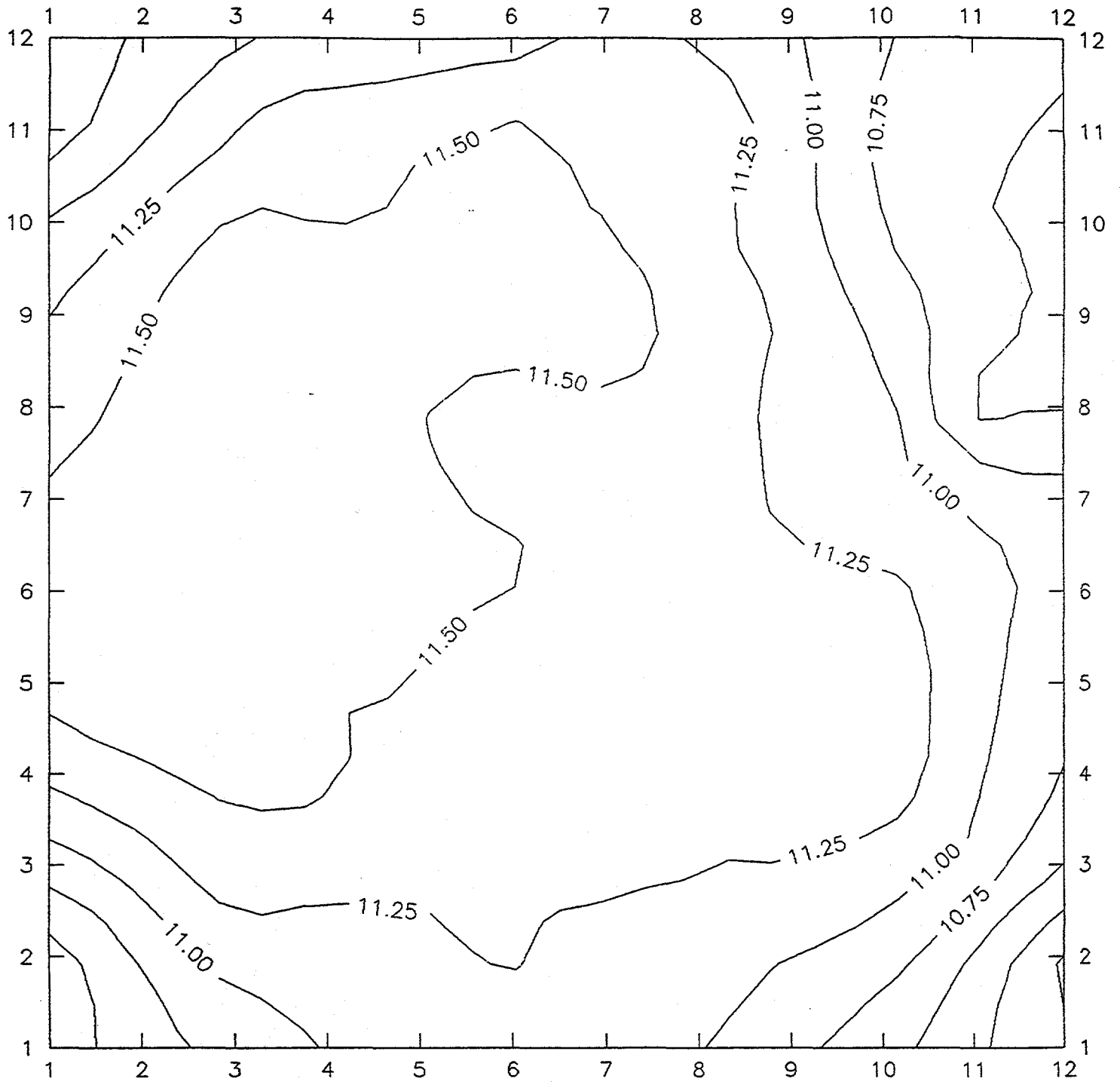
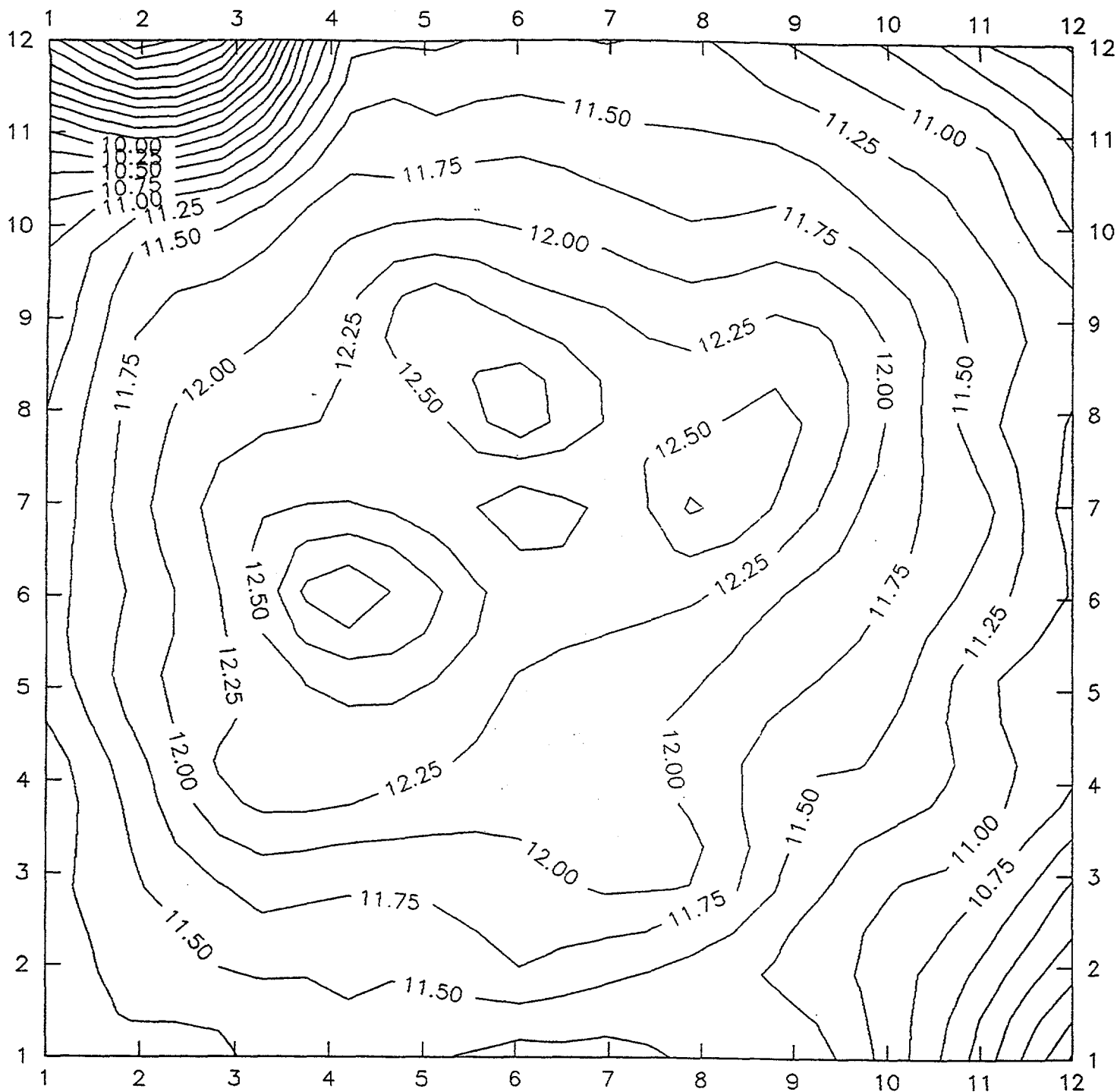**Figure 27.** J_{sc} contour plot of top a-Si:H cell on stainless steel.

Figure 28. J_{sc} under orange filter contour plot of bottom a-SiGe:H cell.

Section 5

Energy Delivery from Double-junction Modules

Introduction

The most important module or system performance parameter is obviously the total energy delivered by the module or system. Unfortunately, site-dependent energy delivery is a very difficult performance parameter to predict. Therefore, the question becomes how can we predict site-specific energy delivery. One way is to simply multiply the one-sun efficiency by the total irradiance delivered at any site. This can be, however, a rather gross approximation. Once a proper model is established, we then, from a manufacturer's point of view, need to evaluate how a module design affects this energy delivery.

The energy delivered by a module will depend upon its response to intensity (G), temperature (T), spectral distribution (E(λ)) and stability (S). Some of the module design characteristics affecting energy delivery are grid patterning schemes, encapsulations and for multijunction module design, choice of band-gaps, layer thicknesses and current matching. We have studied the effect of current matching on energy delivery from multijunction modules. The results are reported in this section.

Methodology

For this study, we have prepared a series of two band-gap, double-junction amorphous modules having an a-Si/a-Si:Ge structure. These modules were fabricated with a grid designed for one-sun operation, with the bottom junction identical for all modules and were approximately 900 cm^2 in size. The only difference between these modules was the top cell thickness, which was adjusted to achieve a current matching ratio between 0.75 and 1.05. The current matching ratio was defined as

$$I_m = \frac{I_{top} (V_{top} = 0)}{I_{bottom} (V_{bottom} = 0)}$$

where I_{top} and I_{bottom} are the short-circuit currents of the top and bottom cell, respectively. These quantities were determined experimentally from quantum efficiency measurements. The module output powers were determined using a portable I-V tracer, and irradiance level was determined with a pyronometer.

To evaluate these results, we needed to define two quantities. The first was called the power efficiency, defined as

$$\eta_p = \frac{P(t)}{Irr(t)}$$

where P(t) and Irr(t) are the instantaneous power and irradiance. This quantity was determined by a solar simulator as would be used by manufacturing to predict module performance. The second quantity, the energy efficiency, was defined as

$$\eta_E = \frac{\int_{day} P(t)dt}{\int_{day} Irr(t)dt}$$

where the numerator is the module output energy for the day, and the denominator is the energy incident upon the module over the course of a day. The energy rating factor R_E is then simply defined as the ratio of the energy efficiency, determined outdoors, to the power efficiency, determined under the solar simulator. That is

$$R_E = \frac{\eta_E}{\eta_{Sim}}$$

As we described earlier, the module energy output is dependent on four primary variable, i.e., intensity, temperature, stability and spectrum. The dependence of module output on current matching was found to be independent of intensity, temperature, and over the short measurement time of this study, stability. The intensity and temperature dependence was determined in separate studies. The stability was believed to be independent over the interval time of this study based on the result that the ratio of power efficiency before and after the conclusion of this study was nearly identical. This leaves any functional dependence of the output power of these modules on current matching only dependent on the spectral content of the irradiance on the days we studied.

Table 17 summarizes the four daily conditions these modules were evaluated under. The first was a partly cloudy/hazy day in which we evaluated both the tracking and fixed tilt cases. The average irradiance level, defined as the total integrated irradiance divided by the number of hours, was 816 and 616 W/m^2, respectively. The second day was at very low irradiance as indicated by the 173 W/m^2 average irradiance level. The third day was very high irradiance at an average irradiance of 708 W/m^2.

Table 17.   Summary of the Four Daily Conditions under which the Test Modules Were Evaluated.

Conditions			Avg. Irradiance Level
Day 1	-	Partly Cloudy/Hazy	
		Tracking	816 W/m^2
		Fixed Tilt	616 W/m^2
Day 2	-	Overcast	
		Fixed Tilt	173 W/m^2
Day 3	-	Clear	
		Fixed Tilt	708 W/m^2

Results

We can see the power efficiency dependence on the current matching ratio in Fig. 29. Note the efficiency under the simulator peaks at a current matching ratio of about 0.95. The efficiency of this module was about 9.3%, demonstrating that state-of-the-art modules were used in this study.

Figure 30 shows the energy rating factor for the four daily cases, described earlier as a function of the current matching ratio. The value of the current matching ratio is shown in the legend. We can see from this graph that on any given day the difference in energy rating factor between any of the modules was minimal. This has very practical implications for optimizing and manufacturing multijunction modules. What this data says is that the energy delivered outdoors by these modules tracked one another in terms of the power they delivered under indoor conditions. In a simple way, this means that if a manufacturer found that of two modules, say A and B, that A had X% higher output under a simulator, and the only difference between module A and B was the degree of current matching, that module A would deliver X% more energy outdoors than module B.

Figure 31 shows the energy rating factor for three different irradiance levels for the fixed-tilt case. Again, the legend shows the current matching ratios for these modules. There are two interesting results here. The first is that the energy rating factor is greater than or equal to unity. This means that the simulator underestimated the energy delivered by these modules. The second is that the energy rating factor increased for decreasing irradiance level. This trend is true because of the relatively high bulk series resistance of amorphous silicon modules, and as the current density is reduced, the efficiency increases. We see this trend at the cell level as well as the module level, indicating this is not an I^2R loss in the module itself.

These results are contrary to results published by other groups that predict amorphous modules would have energy rating factors considerably less than unity, and in some locations as much as 20% lower than unity. We believe this is due to the test samples that were used in these studies having poor response to lower intensities due to being significantly shunted. We have found that all modules and cells (degraded or undegraded) with high shunt resistance (unshunted) exhibit no such response, and, in fact, have energy rating factors greater than unity.

Initial SRC Efficiency vs Current Matching
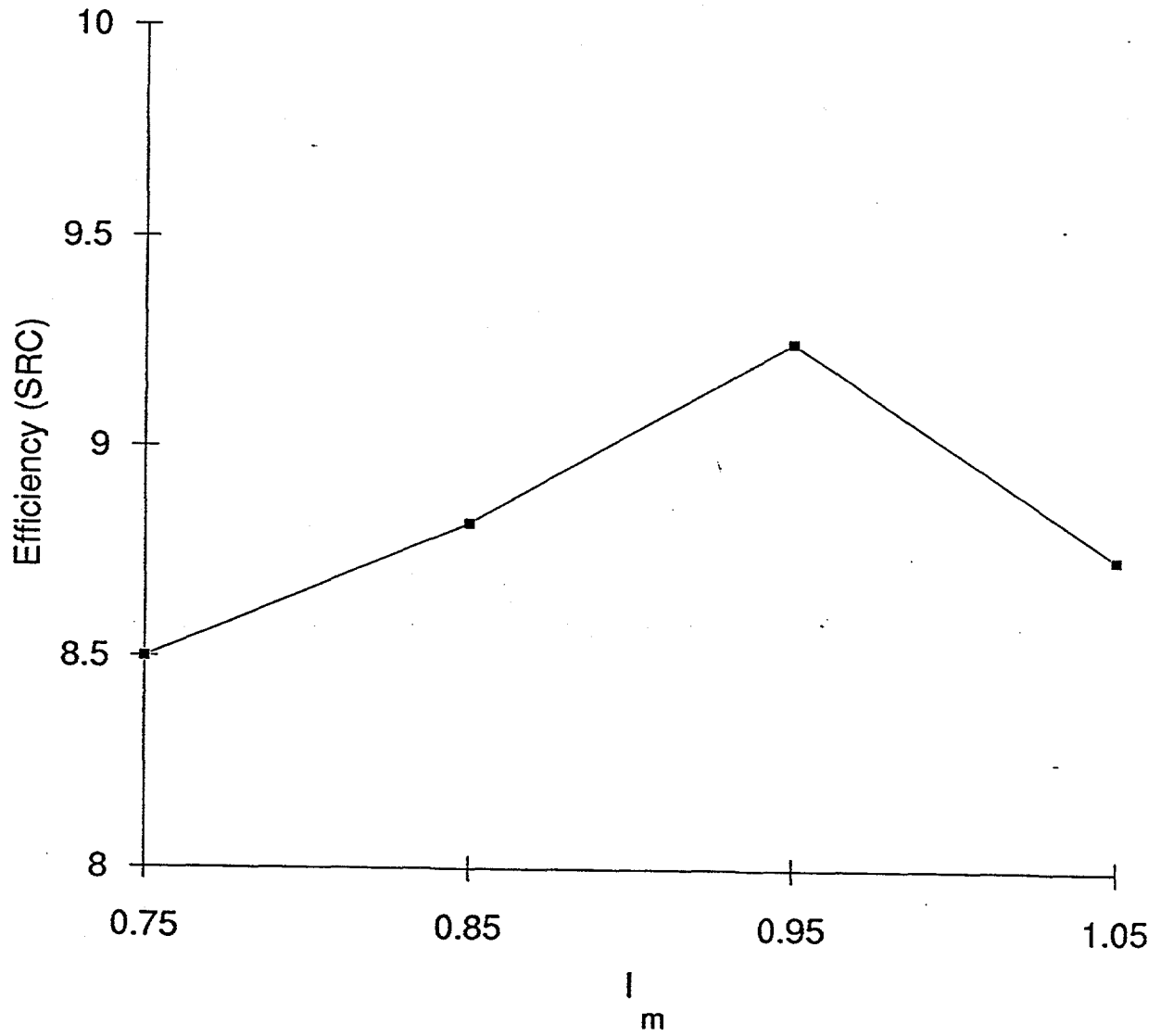
Figure 29. The initial standard reporting condition efficiency versus the module current matching ratio.

Energy Rating Factor for 4 Cases
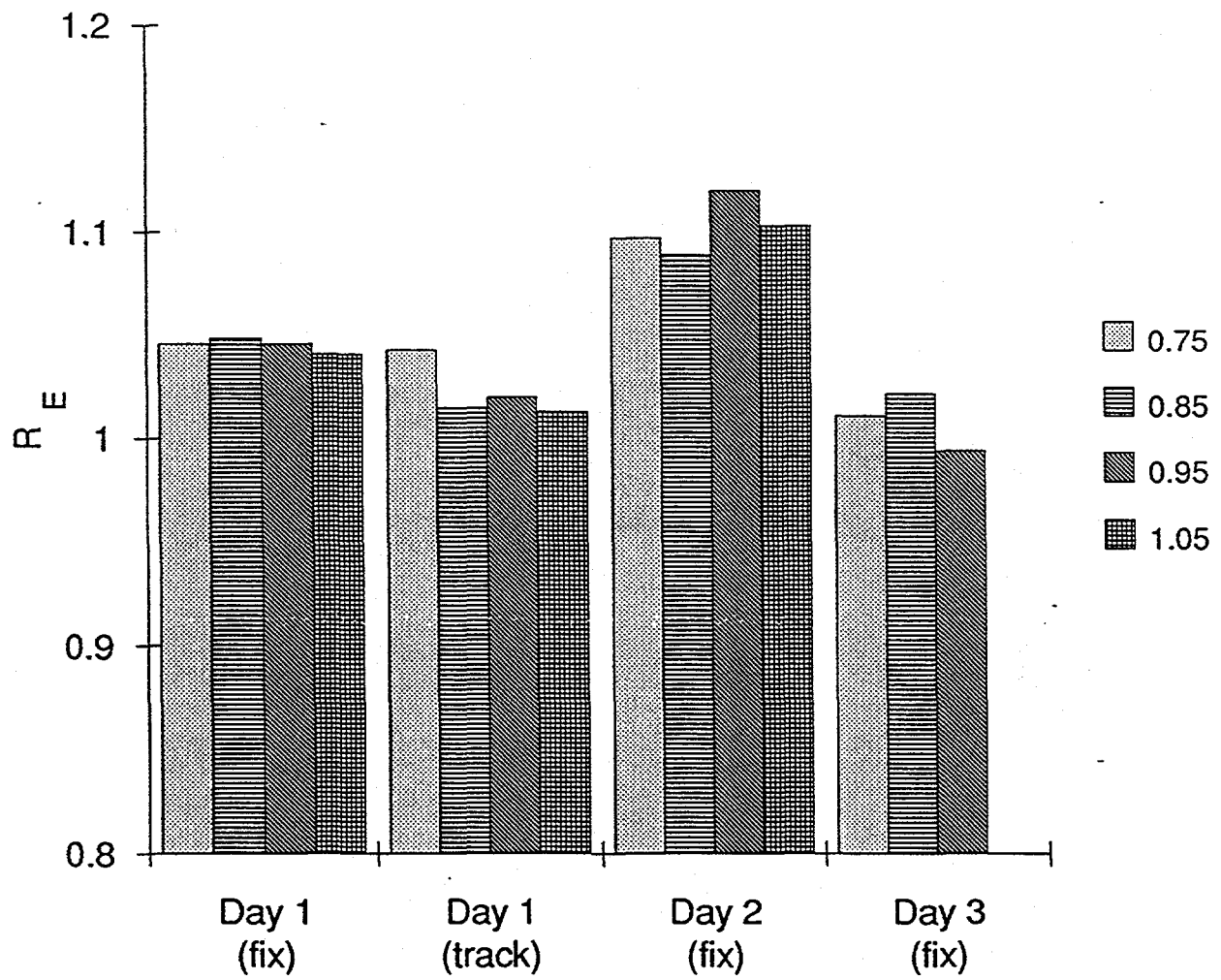

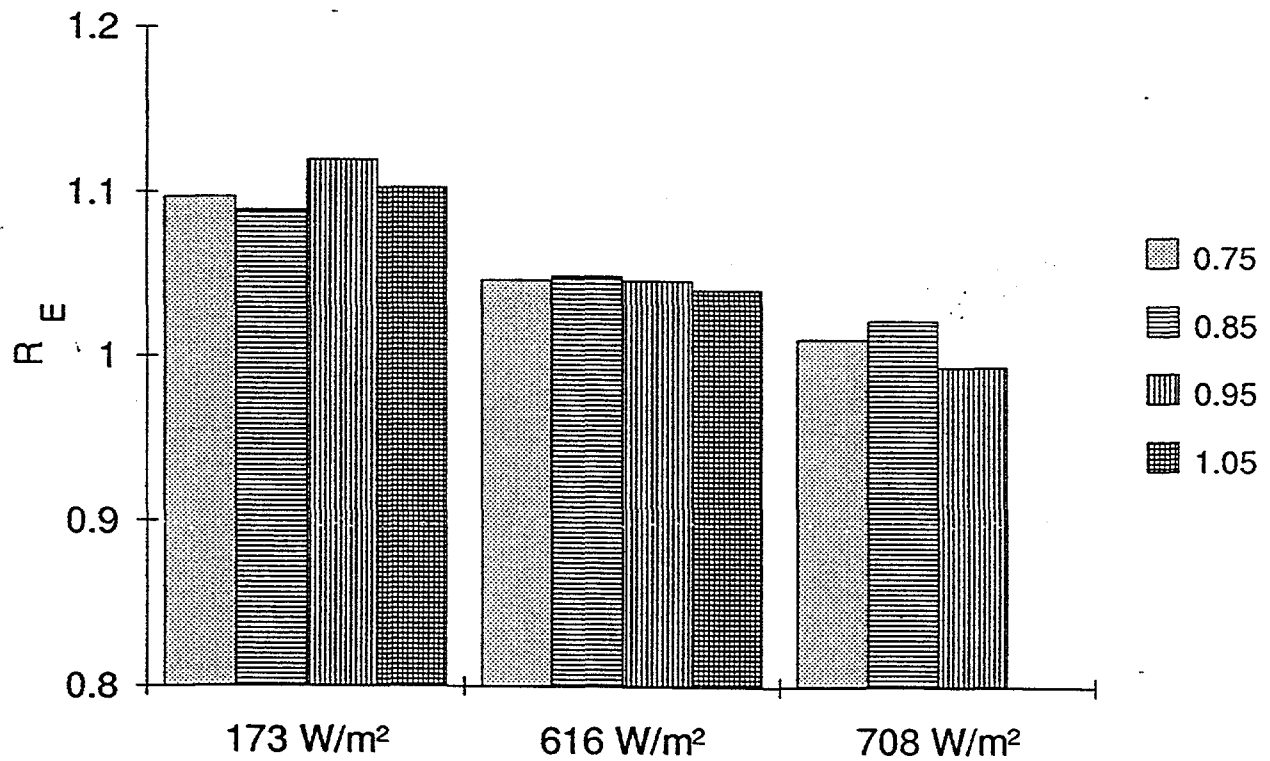**Figure 30.** The energy rating factor for the four daily cases as a function of the module current matching ratio.

Figure 31. The energy rating factor versus irradiance level and module current matching ratio for the fixed tilt case

Section 6

Conclusions and Future Directions

During the period under review, significant advances have been made in obtaining higher efficiency in double-junction modules. In a period of 14 months, the highest initial efficiency achieved has increased from 8.2% to 10.6%. The improvement has been obtained through a combination of i) optimization of the individual intrinsic layers, ii) reduction in the losses at the "tunnel" junction and iii) lowering the grid and encapsulation losses. Simultaneously, through a series of fundamental studies, important information has been obtained on the microstructure of the materials and its effect on cell performance. Microstructure is found to have a profound effect not only on initial cell efficiency but also on light-induced degradation.

The stabilized efficiency of the modules made during this phase is in the range of 8% to 9%. As we have discussed earlier, uniformity studies on the cells deposited over a large area show a 5% difference in the efficiency in the central 450 cm^2 area and that over the entire deposition area of about 950 cm^2. Optimization is in progress now to obtain better uniformity, and this will lead to improvement in module efficiency. The highest stabilized small-area efficiency obtained in the 2B machine is still about 5% to 10% lower than that obtained in the small-area deposition machine (LINE). We believe that through a continuous process of optimization, the gap will be narrowed, and once cells from the 2B machine reach the level of 11% small-area stabilized efficiency as achieved in the LINE machine, 10% stabilized module efficiency is a real possibility. Moreover, further gain in stability will come from triple-junction structures which will be one of the focuses of our attention in Phase III of this program.

References

1. H. Deckman, C. Roxlo, and E. Yablonovitch, Optics Letters 8, 491 (1983).

2. A. Banerjee and S. Guha, J. Appl. Phys. 69, 1030 (1991).

3. J. Burdick and T. Glatfelter, Solar Cells 18, 301 (1986).

4. H.A.M. MacLeod, in *Active and Passive Thin Film Devices* (Academic Press, New York, 1978).

5. R. Edgerton and D. Shortt, Nat. Bur. Stand. (U.S.), Spec. Publ. 697 (1985).

6. V. Nangia, H. Soonpaa, and B. Sesh Rao, J. Opt. Soc. Am. 72, 232 (1982).

7. W.D. Daniels, *An Introduction to Numerical Methods and Optimization Techniques.* (North-Holland, New York, 1975).

8. A. Smith, A. Rohatgi, and S. Neel, Proceedings of 21st IEEE Photovoltaic Specialists Conference (1990).

9. For recent publications on this subject, see *Amorphous Silicon Materials and Solar Cells*, edited by B. L. Stafford (American Institute of Physics Conf. Proc. 234, New York, 1991).

10. S. Guha, J. Yang, W. Czubatyj, S. J. Hudgens and M. Hack, Appl. Phys. Lett. 42, 588 (1983).

11. C. R. Wronski and N. Maley, in *Amorphous Silicon Materials and Solar Cells*, edited by B. L. Stafford (American Institute of Physics Conf. Proc. 234, New York, 1991), p. 11.

12. D. L. Williamson, A. H. Mahan, B. P. Nelson and R. S. Crandall, J. Non-cryst. Solids, 114, 226 (1989).

13. A. H. Mahan, D. L. Williamson, B. P. Nelson and R. S. Crandall, Phys. Rev. B 40, 12024 (1989).

14. A. H. Mahan, D. L. Williamson, B. P. Nelson and R. S. Crandall, Solar Cells, 27, 465 (1989).

15. S. Guha, Final Report, SERI/TP-211-3918 (Solar Energy Research Institute, Golden, Colorado, 1990).

16. D. L. Williamson, A. H. Mahan, B. P. Nelson and R. S. Crandall, Appl. Phys. Lett. 55, 783 (1989).

17. A. Guinier, *X-ray Diffraction in Crystals, Imperfect Crystals and Amorphous Bodies* (W. H. Freeman, San Francisco, 1963), p. 264.

18. E. Bhattacharya and A. H. Mahan, Appl. Phys. Lett. 52, 1587 (1988).

19. A. Langford, M. Fleet, B. P. Nelson, W. A. Lanford and N. Maley, Phys. Rev. B45, 13367 (1992).

20. A. Matsuda, S. Mashima, K. Hasezaki, A. Suzuki, S. Yamasaki and P. J. McElheny, Appl. Phys. Lett. 58, 2494 (1991).

21. W. Den Boer and S. Guha, J. Appl. Phys. 57, 5539 (1985).

22. M. Stutzmann, W. B. Jackson and C. C. Tsai, Phys. Rev. B 34, 63 (1986).

23. S. Guha, C. Y. Huang and S. J. Hudgens, Appl. Phys. Lett. 45, 50 (1984).

24. R. S. Crandall, Phys. Rev. B 43, 4057 (1991).

25. W. B. Jackson and N. M. Amer, Phys. Rev. B 25, 5559 (1982); M. Vanecek, J. Kocka, J. Stuchlik, Z. Kozisek, O. Stika and A. Triska, Sol. Energy Mat., 8, 411 (1983).

26. X. R. Li, S. Wagner and M. Bennett, Mat. Res. Soc. Symp. Proc. Vol. 258, p. 899 (1992).

27. See, for example, N. W. Wang, X. Xu and S. Wagner, in Ref. 1, p. 186.

28. S. Guha, J. S. Payson, S. C. Agarwal and S. R. Ovshinsky, J. Non-cryst. Solids, 97 & 98, 1455 (1988).

29. S. Guha, J. Yang, S. J. Jones, Y. Chen and D. L. Williamson, Appl. Phys. Lett. 61, 1444 (1992).

30. Q. Wang, H. Antoniadis, E. A. Schiff and S. Guha, Mat. Res. Soc. Symp. Proc. Vol. 258, p. 881 (1992).

31. J. Yang, R. Ross, T. Glatfelter, R. Mohr, and S. Guha, Mat. Res. Soc. Symp. Proc. Vol. 149, p. 435 (1989).

32. S. Guha, J. Yang, A. Pawlikiewicz, T. Glatfelter, R. Ross, and S. R. Ovshinsky, Appl. Phys. Lett. 54, 2330 (1989).

Document Control Page	1. NREL Report No. NREL/TP-411-5654	2. NTIS Accession No. DE93010046	3. Recipient's Accession No.

4. Title and Subtitle Research on Stable, High-Efficiency Amorphous Silicon Multijunction Modules	5. Publication Date July 1993
	6.

7. Author(s) S. Guha	8. Performing Organization Rept. No.

9. Performing Organization Name and Address United Solar Systems Corporation Troy, Michigan	10. Project/Task/Work Unit No. PV241101
	11. Contract (C) or Grant (G) No. (C) ZM-1-19033-2 (G)

12. Sponsoring Organization Name and Address National Renewable Energy Laboratory 1617 Cole Blvd. Golden, CO 80401-3393	13. Type of Report & Period Covered Technical Report 1 January 1992 - 28 February 1993
	14.

15. Supplementary Notes
NREL technical monitor: W. Luft

16. Abstract (Limit: 200 words)

This report describes the progress made during Phase II of the R&D program to obtain high-efficiency amorphous alloy multijunction PV modules. The highlight of the work includes: (1) demonstration of world-record small-area efficiency of 11.2% after one-sun light-soaking at 50°C for 600 h using a dual band gap, double-junction structure; and (2) demonstration of initial module efficiency of 10.6% over 0.09-m^2 (1-ft^2) area using the same double-junction approach. In addition, fundamental studies on material properties and cell performance showed an interesting correlation between microstructure in the material and cell efficiency both in the initial and light-degraded conditions.

17. Document Analysis
a. Descriptors
   high-efficiency ; amorphous silicon ; multijunction ; modules ; photovoltaics ; solar cells ; PV

b. Identifiers/Open-Ended Terms

c. UC Categories
   271

18. Availability Statement National Technical Information Service U.S. Department of Commerce 5285 Port Royal Road Springfield, VA 22161	19. No. of Pages 72
	20. Price A04

Form No. 0069E (6-30-87)